# AU/PT MULTILAYERS FORMED BY COLD ROLLING

# THERMAL STABILITY AND PHASE EQUILIBRIUM OF AU/PT MULTILAYERS FORMED BY REPEATED COLD ROLLING

By

YAN SUN, B.ENG.

A Thesis

Submitted to the School of Graduate Studies

in Partial Fulfillment of the Requirements

for the Degree

Master of Applied Science

McMaster University

MASTER OF APPLIED SCIENCE (2004) McMaster University

(Materials Science and Engineering) Hamilton, Ontario

TITLE: Thermal Stability and Phase Equilibrium of Au/Pt Multilayers formed by Repeated Cold Rolling

AUTHOR: Yan Sun, B.Eng.

SUPERVISOR: Dr. Purdy

CO-SUPERVISOR: Dr. Brooks

NUMBER OF PAGES: xiii, 103

## ABSTRACT

Multilayers provide an ideal tool to study thermodynamics of heterogeneous systems far from equilibrium. In this study, synthesis, characterization, thermal stability and phase equilibrium of multilayers are investigated based on Au-Pt system.

Au-50%Pt multilayers were first formed by repeated rolling and folding. The microstructure was investigated by x-ray diffraction (XRD), scanning electron microscopy (SEM), and transmission electron microscopy (TEM). These methods revealed that the process reduced layer thicknesses to below 30nm. However, delaminating and non-uniform spacings were also observed in some regions. To get well-welded and regular multilayers, the experiment was redesigned. The improved approach, involving repeated cutting, stacking, annealing and cold rolling, has yielded uniform multilayers with interlamellar spacings as low as 6nm. XRD demonstrated *the formation of a homogeneous solid solution* during cold rolling at room temperature. TEM suggested that the multilayers were discontinuously homogenized via steady state motion of boundaries. The reason for the solid solution formation is that the stored interface energy is higher than the energy barrier for solid solution formation.

The solid solution is unstable. It decomposes into Au and Pt after heating to 500°C at 50°C/min by differential scanning calorimetry (DSC).

The phase diagram is strongly modified in the nanometer range when we take into account of interface energy. The grain size dependent phase diagram model of Au-Pt system shows that the melting points of Au and Pt can be lowered more than 300K if the average grain size is reduced to 10nm.

The melting temperature of Au/Pt multilayers has been studied with theoretical and experimental approaches. High speed laser heating was used to minimize any modification of the multilayer structure prior to melting. The qualitative experimental results are shown to be in agreement with expectations.

## ACKNOWLEDGEMENTS

I am indebted to my supervisors, Dr. Purdy and Dr. Brooks for their valuable guidance and encouragement. I wish to express my gratitude for many learning opportunities that they provided me with.

I wish to thank to all students, staff, and researchers who supported me throughout this work, especially Hatem Zurob and Jinichiro Nakano for their friendship, Yan Li and Aleksandra Perovic for their TEM help, Florent Lefevre-Schlick and Andrzej Borowiec for introducing me to laser ablation. Also, much appreciation is owed to the technical staff of the Brockhouse Institute for their assistance in the course of this work. I am particularly grateful to Jim Garrett and Fred Pearson.

I am also grateful for the love and support of my husband Shan Gao and my parents.

# TABLE OF CONTENTS

## LIST OF FIGURES

## LIST OF TABLES

# CHAPTER 1

# LITERATURE REVIEW

## 1.1 Nanostructured Materials

Nanostructured materials (NsM) are materials with a microstructure whose characteristic length scale is on the order of a few nanometers (Siegel, 1994). In this section, a brief overview of thermodynamic properties, synthesis and characterization of NsM will be presented. The microstructure and melting-point depression will be introduced in section (1.1.1). We will restrict attention to mechanical alloying to understand physical deformation, welding and fracture proclivities of powder particles in section (1.1.2). The characterization techniques will be introduced in section (1.1.3).

### 1.1.1 Introduction

(1) Microstructure

Most properties of solids depend on their microstructure, e.g. the phases present, grain size, and crystallographic orientation. Nanostructured materials (NsM) consist of nanometer-sized crystallites and a large volume fraction of coherent and incoherent interfaces( Gleiter, 2000). The microstructure of NsM is crucial for many properties, such

as mechanical properties. The nanophase metals often exhibit significant increase in yield strength and elastic modulus.

(2) Melting Temperature and Phase Diagram

The combination of thermodynamics and kinetics can be used to fundamentally describe the melting behavior of solid. The melting point depression is commonly observed in the nanometer regime. For simplicity, it will be assumed that the small particles are spherical. The free energy, increased by interfacial energy (known as capillarity effect or Gibbs-Thomson effect) is added into the molar Gibbs free energy of solid phase. At equilibrium temperature $T_m$, the molar Gibbs free energies of solid and liquid phase are equal. Thus, we can attain that the change in melting temperature $\Delta T$ is inversely proportional to the radius of the sphere $r$. This can be given by

$$\Delta T = (2V\gamma T_m)/(r\Delta H_m) \tag{1.1}$$

Where $\gamma$ is the surface energy, $\Delta H_m$ is the heat of fusion, $V$ is the molar volume. It can be seen that the melting temperature decreases significantly with decreasing grain size, especially in the nanometer range.

Among others, Wautelet (2000) proposed that the phase diagram of small particles (with diameter in the nm range) is size-dependent. This is the Gibbs-Thomson effect. For the case of ideal solutions, it is shown that the lens-shaped solidus-liquidus curves are shifted to lower temperatures when the dimensions of the particle decrease. At fixed temperatures between the highest and lowest melting points of the small particle,

the relative concentrations of the solid and liquid phases are different in small particle and bulk material.

### 1.1.2 Processing

There are many methods to form nanostructured materials: eg. electrodepositon, crystallization of amorphous solid, mechanical alloying. It is relatively easy to synthesize powders and produce small samples with nanoscaled structures, but it is much more difficult to obtain the same materials in bulk forms large enough for structural applications (Shaw, 2000). Nevertheless, a variety of processing methods have been devised and many have exhibited great potential for the production of bulk nanostructured materials with a grain size less than 100nm. We will first consider the mechanical alloying (MA) method. In section (1.2.1), we will review the process modeling of MA in an attempt to understand the physical deformation, welding and fracture proclivities of powder particles. In section (1.2.2), comparison between cold rolling and ball milling will be given.

#### 1.1.2.1 Mechanical Alloying (MA)

The review by Courtney (1995) for the process modeling of mechanical alloying is recommended. The models predict the general trends of powder particle development during MA. Courtney considers a "typical" collision involving powder trapped between

grinding media and determines the deformation, welding and fraction, which the particle experiences, to provide a "snap shot" of the collision.

For convenience, Maurice considered a grinding media ball to be uniformly coated with powder.

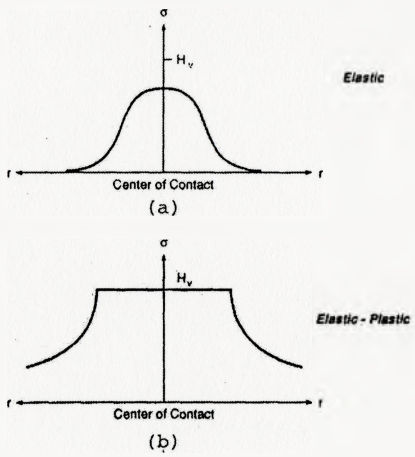


Fig.1.1 The collision stages of powder coated balls. (a) In the early collision stage, the powder deforms elastically; the stress is greatest at the initial contact point. (b) When the stress at the initial contact point attains the powder hardness, plastic deformation initiates there and proceeds outward. Thus, the contact zone is characterized by a plastic cylinder surrounded by an elastic annulus. (Courtney, 1995)

The balls initially deform elastically, and the stress they experience is the greatest at the initial contact point ( Fig.1.1(a)). As the powder proceeds to deform, the stress here eventually attains the powder's yield strength and plastic deformation commences. With continuing deformation, the radius of the plastic zone spreads outward (Fig.1.1(b)). Thus, the powder affected-volume consists of a plastic cylindrical core surrounded by an elastic annulus.

The powder hardness increases during MA due to work hardening. Therefore, the incremental powder strain in successive collisions becomes progressively less. In numerical implementation of the model, the powder hardness is considered constant during a specific collision.

Maurice assumes powder coalescence to take place by cold-welding of plastically deformed particles (Fig.1.2). Plastically deformed particles make metal-metal contact over a fraction of their mating areas. A weld may not survive the elastic recovery associated with the last half of the collision which produces a tensile stress acting to sever the weld. A shear stress also serves to shear the weld. Maurice defines the criterion for weld "survival" as following,

$$\sigma_u^2 A_w^2 \geq N_e^2 + 3T_b^2 \tag{1.2}$$

where, $A_w$ is the area over which metal-metal contact has been made, $\sigma_u$ is the weld tensile strength, $N_e$ is the normal elastic recovery force, and $T_b$ is the comparable shear force. Maurice also considered the presence of dispersoids entrapped between the mating surfaces. The dispersoids impede welding by reducing the area over which metal-metal contact is made.

Criteria for fracture initiation and propagation were also developed. Two methods were developed for determining a fracture initiation criterion. The first predicts that strain is the greatest at the particle circumference. This is thought to be caused by sticking friction and workpiece barreling. Thus, edge fracture initiates there. The second method

disregards sticking friction, and predicts that strain is greatest at the contact center and crack initiation takes place at the particle center. If the initial crack length is less than the powder particle size, the crack must subsequently propagate to effect particle fracture.

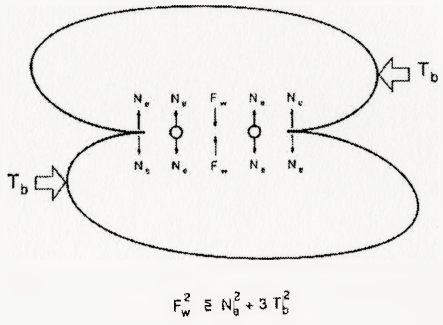


**Fig. 1.2 Schematic illustration of powder cold-welding during MA. Plastically deformed particles make metal-metal contact over a fraction of their mating area. The weld formed may or may not survive the recovery half of the collision; this depends upon the strength of the formed weld relative to the elastic recovery force and the shear force serving to sever the weld. Dispersoids (open circles) act to prevent cold welding. (Courtney, 1995)**

Maurice also considered powder particle shape changes due to particle deformation, cold-welding and fracture. The particle shape factor is doubled by cold-welding and fracture, but is reduced by deformation.

Aikin has undertaken a different approach to local modeling. He described alloying "kinetics" from the standpoint of chemical kinetic principles. Alloying of two ductile materials to form a third (composite or alloy) species is considered (Fig.1.3). Welding and fracture probabilities of the constituent and alloy species are defined and time evolution equations for the species are developed using these parameters. The approach appears different from that of Maurice's. However the main difference between

the approaches is that the fracture and welding probabilities are time dependent in Maurice's treatment, whereas they are considered constant in Aikin's.

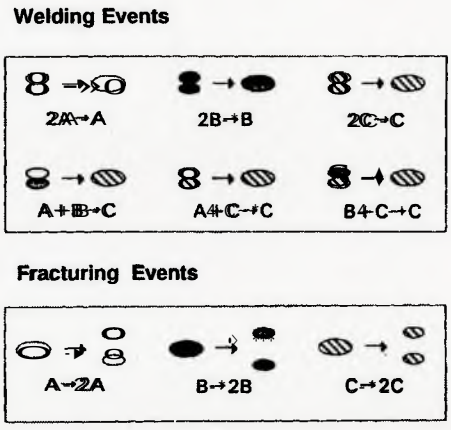


Fig. 1.3 Schema showing how powder particle numbers change as a result of fracture and weld events. A and B are alloyed to form composite C particles. When an A/B particle welds to any other particle, the number of A/B particle is reduced by one. If an A particle welds to a B particle, the number of C particles is increased by one. When two C particles weld, the number of C particles is reduced by one. When any type of particle fractures, the number of that particle species is increased by one.

### 1.1.2.2 Comparison between Cold rolling and Ball Milling

Cold rolling is a technique for mechanical alloying elemental metals. It has weld features in common with ball milling: the metals are sheared together and cold-welded. However, cold rolling is a less energetic process. Usually, the input energy of rolling is not high enough to induce solid-state reactions between the elements, unless diffusive motion of atoms is induced by thermal treatment. In ball milling, a high amount of energy is transferred to the powders in each impact. After a few impacts of the balls (low milling time), the microstructure of the powders is close to those found in cold rolled foils. But with prolonged milling at high energies the comparison is no longer valid, since

intermetallics are formed directly in the vial with no need for further heat treatment. (Battezzati et al, 1999)

### 1.1.3 Measurements and Characterization

Usually, nanostructured materials are characterized using both Transmission Electron Microscopy (TEM) and X-Ray Diffraction (XRD) techniques. Differential Scanning Calorimetry (DSC) and Differential Thermal Analysis (DTA) are used to measure heat transition so as to study thermal stability of the sample or used as precisely temperature controlled annealing furnace.

Microstructure is studied by Scanning Electron Microscopy (SEM), Transmission Electron Microscopy (TEM) or High-Resolution Electron Microscopy (HRTEM). Microtomy techniques can be used to prepare cross-sectional TEM samples of the layer structures. The principle of a microtome is simply the gradual advance towards the cutting knife of a specimen, which is pivoted so that it can be swung past the diamond knife. The advance can be mechanical or thermal, and is controlled to give the desired thickness of slice. The main disadvantage of the technique is the deformation introduced in the specimen during preparation. In other words, the materials deform elastically and plastically due to the geometry of the knife (Hirsch,1965).

The structure of nanostructured materials can be studied by X-ray diffraction at high and low angle regions. Low angle scattering or small angle scattering, with angles $2\theta$

ranging from 0° up to roughly 2 or 3°, can be used to measure the small grain size and to some extent the shape of grains (Cullity, 1977). Moreover, low-angle X-ray diffraction profile can also provide detailed information about the multilayer periodicity and thickness of the individual layers (Vanderstraeten, 1991, Xu, 2001).

Differential Scanning Calorimetry (DSC) and Differential Thermal Analysis (DTA) are used to measure specific heat capacity and heats of transition. They are also used to detect the temperatures of phase changes and melting points. The operation of DSC is based on the measurement of the thermal response of an unknown specimen as compared with a standard when the two are heated uniformly at a constant rate.

## 1.2 Crystal Interfaces

Many solid-state reactions occur at interfaces. In this section, we will only consider the crystal interface boundary, which leads to heterogeneous transformation. A brief review will be given on structures of interface boundary, interfacial free energy, interfacial diffusion and interface migration. The review by Purdy (2002) for transformations involving interfacial diffusion is recommended.

### 1.2.1 Structures of Interface Boundary

The internal surfaces are necessary elements of an equilibrium multiphase system, which are not defects, as grain boundaries. They separate different phases both chemically and structurally. (Purdy and Brechet, 2002)

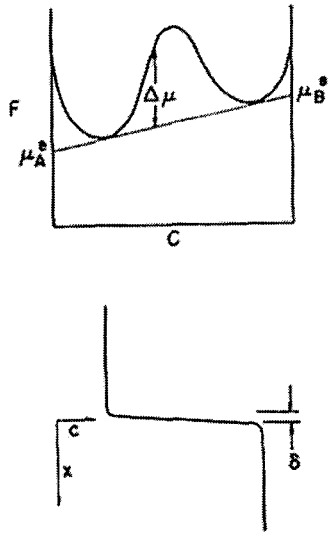


Fig.1.4 Top: A schematic concentration (C) profile through a diffuse coherent interface (components A and B) in which excess chemical free energy, represented by the quantity $\Delta\mu$, is everywhere balanced against gradient free energy (F: free energy, $\mu_A^e$ and $\mu_B^e$: equilibrium chemical potentials). Bottom: Finite thickness $\delta$ of equilibrium interface, corresponding to concentration profile.

The description of an interface dates from the seminal papers by Cahn and Hilliard (1958) and Allen and Cahn (1977). The Cahn-Hilliard model of a stationary coherent interface boundary is illustrated in Fig1.4. The Cahn-Hilliard treatment applies to chemical heterogeneous solids and Allen-Cahn treatment deals with structurally heterogeneous materials. These two classes of problems, coupled with intermediate

situations, cover the range of problems involving relaxed interfaces (Purdy and Brechet, 2002).

### 1.2.2 Interfacial Free Energy

The interface has been arbitrarily restricted to some predetermined thickness in most previous theoretical treatment of interfacial energies (Guggenheim, 1945 and Defay 1950). Cahn (1958) pointed out that the assumption is incorrect in principle, since, once temperature and pressure of the system are specified, the interfacial thickness is no longer an independent variable. Cahn (1958) proposed a new free energy function involving not only the local composition or density, but also those gradient terms compatible with the symmetry of the problem in a nonuniform system, which has a spatial variation in one of its intensive scalar properties, such as composition or density.

The free energy function of a volume $V$ of an isotropic system of nonuniform composition or density is given by

$$N_v \int_v [f_0(c) + \kappa(\nabla c)^2] dV \tag{1.3}$$

where $N_v$ is the number of molecules per unit volume, $\nabla c$ is the composition or density gradient, $f_0$ is the free energy per molecule of a homogeneous system, and $\kappa$ is gradient energy coefficient, which is a function of the local composition and temperature, but for a regular solution is a constant which can be evaluated. The minimum of this integral with respect to a one-dimensional composition or density variation can be used to determine

the free energy of a flat interface between two coexisting phases and specific interfacial free energy.

We will consider a flat interface of area A between two coexisting isotropic phases $\alpha$ and $\beta$ of composition $c_\alpha$ and $c_\beta$. It will be assumed that the free energy of non-equilibrium materials of composition intermediate between $c_\alpha$ and $c_\beta$ can be represented by a continuous function $f_0(c)$ of the form shown in Fig.1.5.

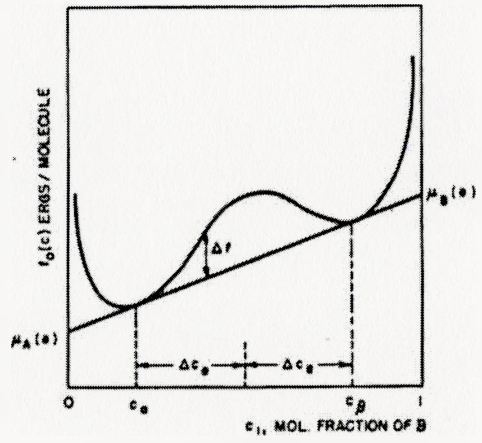


Fig.1.5 $f_0(c)$ for $T < T_c$

Considering the one-dimensional composition change across the interface, and neglecting terms in derivatives higher than the second, we obtain the total free energy $F$ of the system:

$$F = AN_v \int_{-\infty}^{+\infty} [f_0(c) + \kappa (dc/dx)^2] dx \tag{1.4}$$

The specific interfacial free energy, $\sigma$, is by definition of the difference per unit area of a diffuse interface between two concentrations $c_\alpha$ and $c_\beta$, which is given by

$$\sigma = 2N_v \int_{c_\alpha}^{c_\beta} [\kappa \Delta f(c)]^{\frac{1}{2}} dc \qquad (1.5)$$

where $\Delta f(c)$ may be regarded as the free energy referred to a standard state of an equilibrium mixture of $\alpha$ and $\beta$.

The diffuse interface and interfacial free energy are also temperature dependent. The interface thickness increases with increasing temperature and becomes infinite at the critical temperature $T_c$ or at a temperature $T$ just below $T_c$. Interfacial free energy $\sigma$ is proportional to $(T_c - T)^{\frac{3}{2}}$ in the critical region.

### 1.2.3 Interfacial Diffusion

Solid-solid interface often provides exceptionally rapid paths for diffusion. Grain boundary diffusion is well experimentally investigated, yet the mechanisms and the details of grain and interphase boundary diffusion are not fully understood at present. The reviews by Peterson (1983) and Kaur and Gust (1988) for grain boundary diffusion are recommended.

Purdy (2002) briefly summarized the present level of understanding of grain boundary diffusion, listed as below. However, he also pointed out that the correlation of

structure with diffusivity remains incomplete and that much remains to be learned about the fundamental processes of interfacial diffusion in solids.

(a) The activation enthalpy for grain boundary self-diffusion is of order of half that for volume diffusion.

(b) For the low angle symmetric tilt boundary, rates of diffusion are anisotropic, with faster diffusion occurring parallel to the dislocation lines. Undissociated dislocations have higher diffusivities than dissociated ones, the diffusivity increases linearly with dislocation density.

(c) Anisotropic behaviour is also obtained for higher angle symmetric tilt boundaries.

(d) Low angle twist boundaries, composed of screw dislocations, are less efficient in transporting materials than their tilt counterparts.

(e) The mechanism of grain boundary diffusion in close-packed metallic systems is thought to involve vacancy exchange.

Interphase boundary diffusion is less well studied. Kaur and Gust (1988) note that only the Sn-Ge/In system has been extensively studied. The reason may be that the interphase boundaries can support local equilibrium concentration gradients only in the presence of gradients of curvature, temperature or stress. However, the isothermal planar interphase boundary is normally isoconcentrate (Purdy and Brechet, 2002).

### 1.2.4 Forces for Interface Migration

Forces are expressed in terms of a normal force per unit area of interface, and therefore have the units of pressure. Purdy and Brechet (2002) summarized four main forces to drive the interface migration: capillary forces, chemical forces, mechanical forces and frictional forces. In this section, we only consider capillary forces and chemical forces.

(1) Capillary forces:

Capillary forces originate from the systems's tendency to reduce its total interfacial free energy $\sigma A$, where $\sigma$ is the specific interfacial free energy and $A$ is the interfacial area. For constant $\sigma$, the force can be expressed as

$$p_\sigma = K\sigma \tag{1.6}$$

Which is the product of the surface free energy and the interface curvature $K = dA/dV$. For smoothly curved interfaces the curvature is the sum of the reciprocal of the two principal radii of curvature $[(1/r_1)+(1/r_2)]$. For strongly anisotropic or faceted interfaces, an effective capillary force may still be defined through the derivation $dA/dV$, although care must be taken in its formulation. For the special case of an equilibrium particle, the capillary force gives rise to a variation of the specific free energy of the included phases (Purdy, 1971).

(2) Chemical forces

The chemical force for interface migration is given by

$$p_{ch} = \frac{\Delta F_{ch}^{'}}{V_m} \tag{1.7}$$

Where $\Delta F_{ch}^{'}$ is the molar free energy difference acting directly across the interface, and is generally less than $\Delta F_{ch}$, the free energy difference accompanying the complete transformation. The reason is that some fraction of total available free energy is dissipated in the volume diffusion field.

## 1.3. Thermal Stability of Lamellar Structured Materials

One major reason for the current interest in lamellar eutectics as high-temperature compositions is the excellent thermal stability of eutectic microstructures. The faulting mechanism for thermal coarsening of such structures has been studied extensively. However, the thermal stability of lamellar eutectoids, in which discontinuous coarsening is the main mode of coarsening, had not yet been studied to any appreciable extent. In this section, the faulting mechanism of lamellar eutectic is briefly reviewed in section (1.3.1). The microstructure, driving force and diffusion model for discontinuous coarsening are examined in section (1.3.2).

### 1.3.1 Lamellar Eutectics

In lamellar eutectics, the two phases are present as alternating sheet. Graham and Kraft (1966), who investigated the lamellar Al-$Al_2Cu$ eutectics, found that in regions with a well-developed lamellar morphology the structure was very stable, but that all non-lamellar regions coarsened rapidly. Their microstructural observations suggest that coarsening only occurred at lamellar faults. This was supported by theory, coarsening by diffusion limited fault migration: dissolution at lamellar edges and re-precipitation on neighbouring lamellae, and it is the most rapid in those grains where initial lamellar structure is imperfect. The faulting mechanism is shown in Fig.1.6. Weatherly and Nakagawa (1971) have produced a theory for the kinetics of this process.

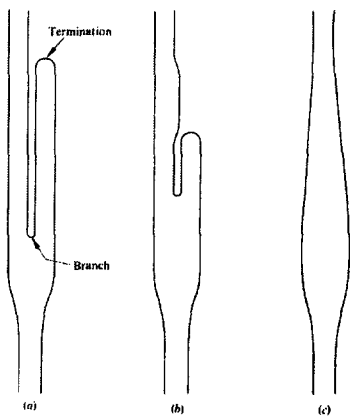


Fig.1.6 Illustrating the instabilities of faults in a rod eutectic. (a) the initial geometry; (b) migration of faults towards each other as the termination shrinks and the branch grows; (c) annihilation of the two opposite faults probably leaving a bulge. (Cline,1971)

### 1.3.2 Discontinuous Coarsening

#### 1.3.2.1 Introduction

The discontinuous coarsening is a reaction during which a fine-lamellar structure created by primary lamellar reaction such as discontinuous precipitation, eutectoid decomposition or eutectic solidification is transformed into a coarser lamellar structure of the same phases,

$$(\alpha_p + \beta)_{fine} \rightarrow (\alpha_s + \beta)_{coarse}$$

Where $\alpha_p$ and $\alpha_s$ are the primary and secondary $\alpha$ phase lamellae respectively, and $\beta$ is the $\beta$ phase lamellae. An idealized model of an elementary cell of a discontinuous coarsening system is presented in Fig.1.7.

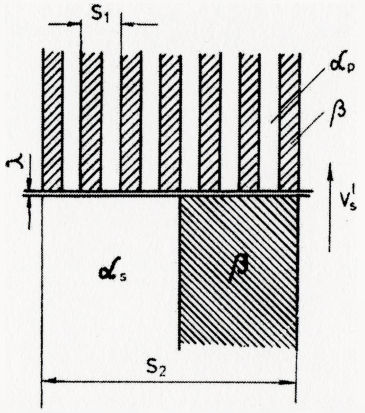


Fig.1.7 Idealized model of the discontinuous coarsening process. Grain boundary moves at rate-$V_s'$ consuming fine lamellar structure with spacing $S_1$ and producing coarse lamellar structure with spacing $S_2$. $\lambda$ is the cells boundary width. (After Cahn, 1974)

A sharp migrating reaction front separates the coarse lamellar reaction product from the fine-lamellar initial state. There is an abrupt change in the orientation and

interlamellar spacing of the $\alpha$ phase across the reaction front. In this way, the process differs essentially from gradual or continuous coarsening, which occurs primarily by fault motion (Pawlowski and Zieba, 1991).

Lamellar microstructures of discontinuous coarsening have been described and discussed by Livingston and Cahn (1974). This is shown in Fig. 1.8 for cobalt-sillicon eutectoid structure transverse to the original growth direction. The process of coarsening occurs only at grain boundaries and involves the migration of boundary, with the coarsening occurring in the growing grain and providing the driving force for the reaction. To this extent it is very similar to discontinuous precipitation. The motion of the grain boundary was into the grain whose lamellae were most nearly normal to the boundary plane as can be seen in Fig.1.8.

Fig.1.8 Transverse section of unidirectionally grown polycrystalline eutectoid Co-Si showing discontinuous coarsening after annealing at 1273K for 96 hours. The lower grain has invaded the upper grain on the left and the upper grain has invaded the lower grain on the right- in both cases the invaded grain has its lamellae most nearly normal to the grain boundary. Note the large ratio (r') of lamellar spacing after growth to that before. (After Livingston and Cahn, 1974).

Livingston and Cahn also analyzed the process on the basis of the driving force as the reduction of interfacial energy and with the principal diffusion path along the grain boundary.

### 1.3.2.2 Driving Force

Livingston and Cahn (1974) first developed the theory of driving force of the discontinuous coarsening, which is given by

$$-\Delta G_s = 2\sigma_c^{\alpha/\beta} v_c \left(\frac{1}{S_1} - \frac{1}{S_2}\right) = 2\sigma_c^{\alpha/\beta}\left(\frac{1}{S_1}\right)\left(1 - \frac{1}{r}\right) \tag{1.8}$$

Where $\sigma_c^{\alpha/\beta}$ is the interphase surface free energy of the fine lamellae, $S_1$ and $S_2$ are the initial and final interlamellar spacings, $r$ is the coarsening ratio, and $v_c$ is the molar volume of cellular aggregate.

Fournelle (1979) pointed out that the theory proposed by Livingston and Cahn (1974) did not describe the chemical free energy remaining after the termination of primary cellular precipitation. Fournelle assumed that the secondary cells grew so slowly that all the remaining energy expressed by $(1 - f_c)\Delta G_0$ was used in the reaction. Hence the driving force for secondary cellular precipitation could be expressed as:

$$\Delta G_s = (1 - f_c)\Delta G_0 + \left(\frac{2\sigma_c^{\alpha/\beta} v_c}{S_2} - \frac{2\sigma_c^{\alpha/\beta} v_c}{S_1}\right) \tag{1.9}$$

Where $f_c$ is the fraction of chemical free energy change released due to primary cellular precipitation, and $\Delta G_0$ is the total available driving force for cellular reactions.

Kaya and Smith (1989) proposed that the strain free energy might be negligible during discontinuous coarsening reactions because the misfit is partially relieved by the formation of interface dislocations and steps. In fact, it is generally observed that periodic dislocation arrays and steps exist between the phases.

The effects of temperature, lamellar orientation and lamellar perfection on the discontinuous process have also been studied. Livingston and Cahn (1974) analyzed the initiation process, and they considered the normal component of the force exerted on the grain boundary by the lamellae to be

$$F_T = \frac{2\gamma \sin^2 \theta}{\lambda_1} \tag{1.10}$$

Where $\gamma$ is the interfacial free energy, $\theta$ is the angle between the lamellae and the grain boundary, and $\lambda_1$ is the spacing of the fine lamellae. The force changes as the function of the lamellar orientation and the force reaches a maximum when the lamellae are perpendicular to the boundary (Kaya and Smith, 1988).

The discontinuous coarsening continued primarily through boundary migration into the grains with more nearly perfect lamellar structures, while continuous coarsening

was most rapid in grains in which the initial lamellar structure was most imperfect (Livingston and Cahn, 1974).

Livingston and Cahn analyzed the Cu-In system and found that discontinuous coarsening is prominent at low temperature, while continuous coarsening effect is more obvious at high temperature.

### 1.3.2.3. Diffusion Model

In developing the diffusion model, Livingston and Cahn (1974) assumed that both fine and coarse lamellae were normal to the planar boundary, which was the only lateral diffusion path. Thus, the steady state condition can be written:

$$D_{b,m}\lambda\left(\frac{d^2C_b}{dX^2}\right) = V_s^l \Delta C \tag{1.11}$$

Where $D_{b,m}\lambda$ is the cell boundary diffusivity, $X$ is the distance along the boundary, $V_s^l$ is the rate of the discontinuous coarsening process, and $\Delta C$ is concentration gradient across boundary. Assuming that the driving force is converted into grain boundary concentration gradient $\Delta C = bC_{b,e}\Delta G_s / RT$ from the Gibbs-Thompson equation, Livingston and Cahn also derived the following equation for the secondary growth rate.

$$V_s^l = \frac{8C_{b,e}}{\left(C_p^\beta - \overline{C}_s^\alpha\right)\left(f_2^\alpha\right)^2\left(f_2^\beta\right)^2}\frac{D_{b,m}\lambda}{(S_2)^2}\frac{\sigma_c^{\alpha/\beta}v_c}{S_1 RT}\left(1-\frac{S_1}{S_2}\right) \tag{1.12}$$

Where $C_{b,e}$ is the equilibrium boundary concentration in the absence of curvature, $v_c$ is the molar volume of cellular aggregate, $f_2^{\alpha}, f_2^{\beta}$ are the volume fraction of secondary $\alpha$ and $\beta$ phases, respectively, $\sigma_c^{\alpha/\beta}$ is the interfacial free energy of cellular aggregate, $R$ is gas constant, $T$ is temperature of the process, $S_1$ and $S_2$ are the interlamellar spacings of the primary and secondary cells, $C_p^{\beta}$ and $\overline{C}_s^{\alpha}$ are the solute concentration in the $\alpha$ and $\beta$ phases.

Moreover, Livingston and Cahn (1974) considered the competition between discontinuous coarsening and continuous coarsening. They compared equation (1.12) with equation of the rate of lamellar faults derived by Cline (1971). The ratio of both rates is proportional to $D_{b,m}\lambda S_1 / D_v (S_2)^2$ where $D_v$ is the volume diffusion coefficient. Assuming that $S_2$ is proportional to $S_1$, this ratio is equal to $KD_{b,m}\lambda / D_v S_1$, where $K$ is the proportionality constant. As the ratio $D_{b,m}\lambda / D_v$ increases generally with decreasing temperature, so discontinuous coarsening prevails at lower temperature and at small interlamellar spacings of the primary cells.

### 1.4. Multilayers

Hilliard and his co-workers have studied multilayers for critical experiments since 1954. Multilayers provide an ideal tool for study of the thermodynamics and kinetics of the heterogeneous system far from equilibrium. In this section, theoretical approach to

possible mechanisms for multilayer homogenization and interface-diffusion-controlled reaction is examined in section (1.4.1). Critical experiments for the formation of regular multilayers by repeated cold rolling are reviewed in (1.4.2).

### 1.4.1 Theoretical Approach

Beginning with an A-B multilayer grown on a bicrystalline substrate such that a grain boundary penetrates the whole structure and provides a possible fast diffusion path, two classes of problems can be developed: (1) A and B are fully miscible, multilayers are discontinuously homogenized via coupled grain boundary diffusion and migration; (2) A and B are reactive, and form a stoichimetric compound (or conversely, when such a compound decomposes to form A and B) by interface-diffusion-controlled reaction.

#### 1.4.1.1 A and B being Fully Miscible

The simplest case occurs if A and B are fully miscible. Grain boundary migration can lead to homogenization by a cooperative mechanism or a "fingering solution" at the former A/B interfaces. Three possible patterns emerge as illustrated in Fig.1.9. (Klinger et al., 1997).

(c)

Fig.1.9 illustrating three different possibilities for the discontinuous homogenization of a monophase multilayer containing a mobile grain boundary, assumed initially to bisect the multilayer. Situations corresponding to (a) the steady state motion of the boundary; (b) an initially sinusoidal instability of the grain boundary; (c) is the "fingering" instability of the moving boundary, after Klinger et al (1997).

The first, the moving boundary adopts a constant velocity and shape, while leaving in this wake a reduced, but in general finite segregation amplitude (Fig.1.9 (a)). The second, the moving boundary adopts a sinusoidal morphology with increasing amplitude (Fig.1.9 (b)). The third, unidirectional non steady states are shown in Fig.1.9 (c). Due to higher imposed thermodynamic driving force, the regions are locally homogenized by "fingers" of grain boundary, leading to strips of homogenized material alternating with unaltered layers of A and B.

Klinger et al (1997) considered the unidirectional process (Fig.1.9 (a) and (c)). The shape of the moving boundary, as well as its velocity and the concentration profile left in its wake, are computed in terms of driving forces, interface energies and diffusion coefficients. We will follow the theoretical approach of Klinger et al for the flat interface

(Fig1.9 (a)) to attain the shape, concentration profile, and velocity of moving grain boundary.

The motion of the grain boundary is given by:

$$V = M(G - \Gamma) \tag{1.13}$$

where $M$ is local grain boundary mobility (assumed constant for given temperature), $G$ is the local free energy difference across the boundary, and $\Gamma$ is a capillary force representing the Gibbs Thomson correction related to the curvature of the interface.

We follow Cahn's (1959) procedure for the determination of grain boundary concentration profiles in discontinuous precipitation and write:

$$V = M\Delta G_0 Q(a) \tag{1.14}$$

$$a = Vd^2 / D\delta \tag{1.15}$$

where $d$ is the thickness of the layers, $D$ is the diffusion coefficient along the grain boundary, $M$ is its mobility and $\delta$ its thickness. $a$ is so called " Cahn parameter" for the moving grain boundary, and $Q(a)$ corresponds to the fraction of available free energy still retained after the sweeping by the moving grain boundary. To get an exact solution required the computation of the shape of the moving grain boundary, since the grain boundary interface is indeed not flat. Klinger, Brechet and Purdy (1997) gave a full numerical treatment. The geometry of the moving grain boundary in the multilayers is shown in Fig.1.10. $\theta$ is the local angle between the grain boundary normal and the Y direction.

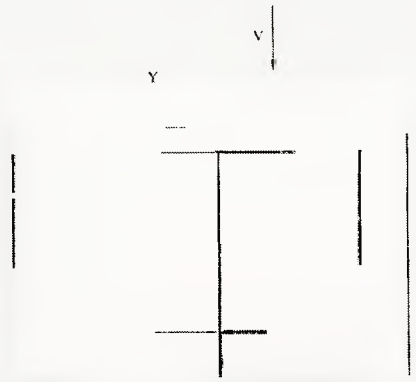

Fig.1.10 Geometry of the moving grain boundary in the multilayers. Left behind the grain boundary is a partially homogenized material: the A/B interface has disappeared and has been replaced by a concentration profile.

To facilitate the study of equations, we use dimensionless parameters, $\alpha^{'}, \beta^{'}, \alpha$ and $\beta$. And $\alpha^{'} = 12\alpha$, and $\beta^{'} = \beta/12$. The dimensionless parameter $\alpha^{'}$ and $\beta^{'}$ is defined as

$$\alpha^{'} = \frac{gd}{\gamma} \tag{1.16}$$

$$\beta^{'} = \frac{M\gamma^2}{Dg\delta} \tag{1.17}$$

where $g$ is the constant of proportionality, and $\gamma$ is the grain boundary energy. Increasing $\alpha^{'}$ can be realized experimentally by increasing the thickness of the layers. Decreasing $\beta^{'}$ means increasing grain boundary diffusivity.

The main results for the constant shape case are presented graphically in Fig.1.11, and it shows the concentration distributions behind the moving boundary and corresponding boundary shapes for different value of $\alpha'$ and $\beta'$.

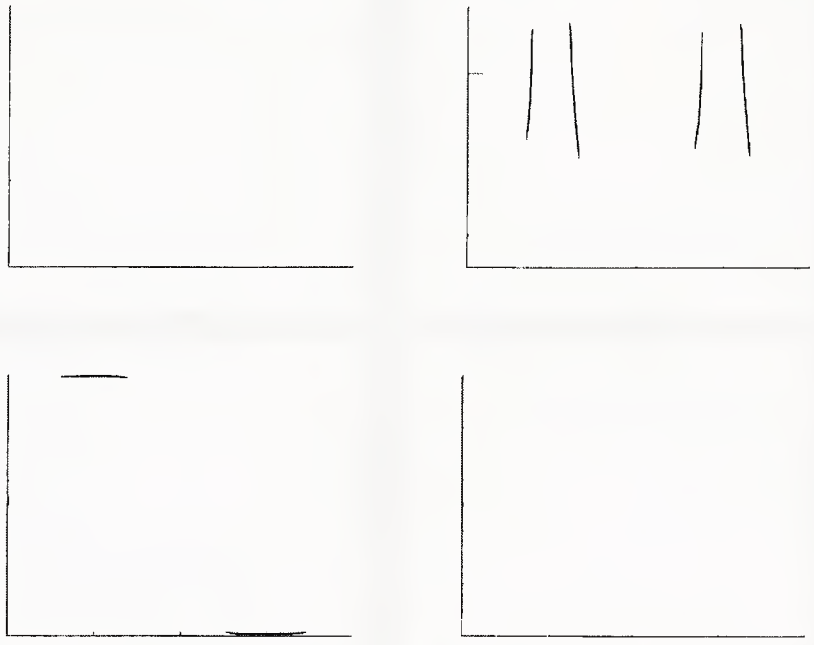

Fig.1.11 Grain boundary shape (a) and (c) and concentration profiles (b) and (d) left behind for steady state moving grain boundary for different values of $\alpha'$ and $\beta'$, after Klinger, Brechet and Purdy (1997).

For bigger values of $\alpha'$, the layers will be larger and migration process slower. Under these conditions, the moving interface becomes more deeply cusped. For small $\alpha'$, (small layer thickness) the concentration profile is flatten, corresponding to an almost complete homogenization. If the layer thickness is increased, the concentration profile reflects a partial homogenization in the region close to the position of the initial A/B interface.

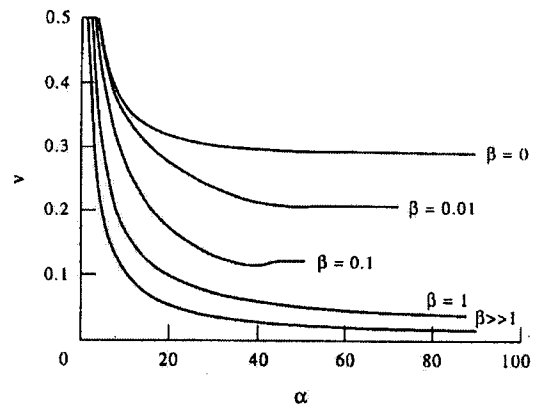


Fig.1.12 Velocity of the moving grain boundary with a steady state shape, as a function of $\alpha'$ for different values of $\beta'$, after Klinger, Brechet and Purdy (1997).

The corresponding velocities for the steady state shapes are shown in Fig.1.12. For small $\alpha'$, the high driving force is due mainly to capillary force, and this leads to high velocities. The line $\beta' = 0$ corresponds to infinitely fast diffusion along the grain boundary, which leads to a concentration everywhere equal to 0.5. The opposite case ($\beta' >> 1$) corresponds to the absence of diffusion and the initial concentration profile is retained.

Klinger, Brechet and Purdy (1997) also studied morphologies and concentration profiles, and obtained predictions for the diffusional fingering case. The results show that the concentration through the finger is nearly constant. When the diffusivity is increased ($\beta'$ decreases), both the velocity and the thickness of the finger increase.

The current treatment is obviously limited to established kinetic states, and it does not answer the question of the stability of the solution, nor does it deal with initiation

transient. Indeed, it is not clear how the migration/homogenization process might begin. It is open to experimental investigation.

### 1.4.1.2 A and B being Reactive

The second situation to be considered is when A and B are reactive, and form a stoichimetric compound or conversely, when such a compound decomposes to form A and B. The velocity of the cooperative moving front is the function of the energies and mobilities involved (Klinger et al., 1997). A solution involving a reaction product layer at the interface rather than a cooperative growth front can also be considered (Fig.1.13).

Fig.1.13 Schematic representation of the possible reactions of A and B to form a stoichiometric product phase $\omega$. (a) A cooperative reaction at a single front; (b) the growth of product layer at the interface (after Klinger et al., 1997).

Although many theoretical investigations required experimental confirmation, they suggest a wide variety of possible kinetic paths toward thermodynamic equilibrium, as well as morphological instabilities, in well-controlled systems.

### 1.4.2. Experimental Work

Perepezko (2001) and Yasuna (1997) used different approaches: repeated cold rolling and folding; repeated cut-stack-anneal-press-anneal-rolling respectively, to form multilayers. The detailed experimental procedure and relevant experimental results will be reviewed.

#### 1.4.2.1 Repeated Cold Rolling and Folding

Fig.1.14 Schematic illustration of repeated cold rolling/ folding experimental procedure.

Multilayers of nickel and aluminum with the composition of Al-20at %Ni and Al-25at% Ni were prepared by the repeated cold rolling and folding (R&F) of elemental foils as shown in Fig.1.14. The main experimental procedure was performed as following: foils of pure elements of Ni and Al with a thickness between 7.5 and 50 μm were stacked to form an array of the selected composition and then folded four times to a 10mm×10mm multilayer sandwich. The sample weight was typically about 0.5g. The folded samples were rolled in a manual rolling machine at a strain rate of $0.1s^{-1}$ to a thickness of approximately 80 μm to obtain the starting material. A small piece of the sample (20~40μg) was retained for examination and the other part was folded to double the

thickness and rolled (R&F) to 80 μm for 10 cycles. The final material was rolled up to 70 passes. Special care was taken during rolling to maintain a clean environment and clean tools.

The rolling procedure results in a decrease in thickness of the elemental layers to below 0.1μm and a reduction in grain size to below 50nm, but does not induce the formation of an intermediate phase.

Battezzati and Gallino (1999) have done the similar work, using repeated cold rolling/ folding to form Al/Ni multilayers.

### 1.4.2.2 Repeated Cut-Stack-Anneal-Press-Anneal-Rolling

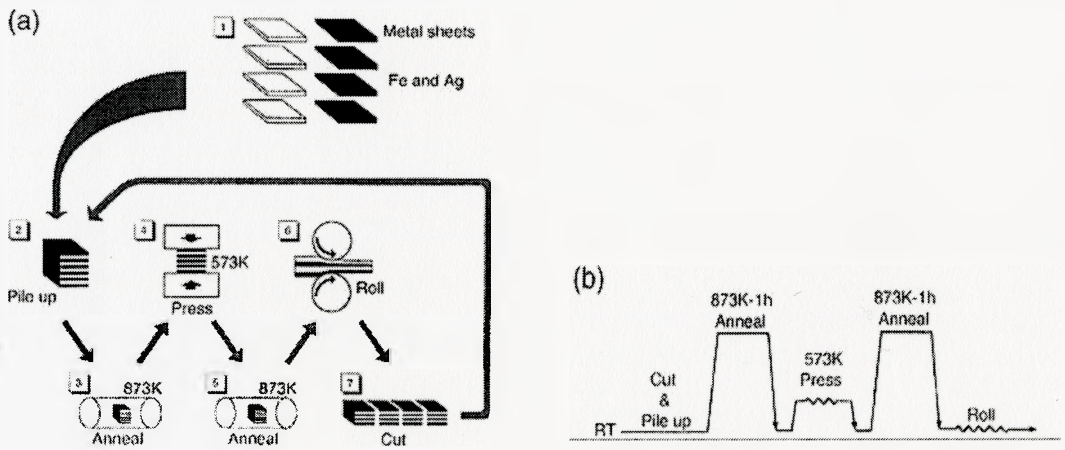


Fig.1.15 Schematic illustration of repeated press-rolling: (a) operations of the press-rolling cycles; (b) temperature profile throughout the cycles ( after Yasuna,1997).

The repeated cut-press-rolling experimental procedure used by Yasuna to form Fe/Ag multilayers was performed as illustration in Fig.1.15. Yasua used "cut and stack" instead of "fold" by comparison with Perepezko's work. Moreover, he mentioned that primary annealing results well-welded metal layers and the annealing between rolling cycles removes strain and defects. Cross-sectional TEM images (Fig.1.16) clearly demonstrated that the very regular multilayers were fabricated. The average layer thickness is about 10nm.

Fig.1.16 Cross-sectional TEM images for Fe/Ag multilayers prepared by the repeated press-rolling of three cycles: (a) lower magnification image (b) higher magnification image (Yasuna,1997).

## 1.5 The Au-Pt System

### 1.5.1 Equilibrium Phase Diagram

The equilibrium phases of the Au-Pt system are: (1) the liquid L, the melting points of Au and Pt are accepted as 1064.43°C and 1769°C; and (2) the fcc, continuous

solid solution (Au,Pt), encompassing a miscibility gap (Au) + (Pt). The critical point of the miscibility gap is at about 61at%Pt and 1260°C. $Au_3Pt$, AuPt, and $AuPt_3$ phases are metastable phases. The equilibrium phase diagram of Au-Pt system is shown in Fig.1.17.

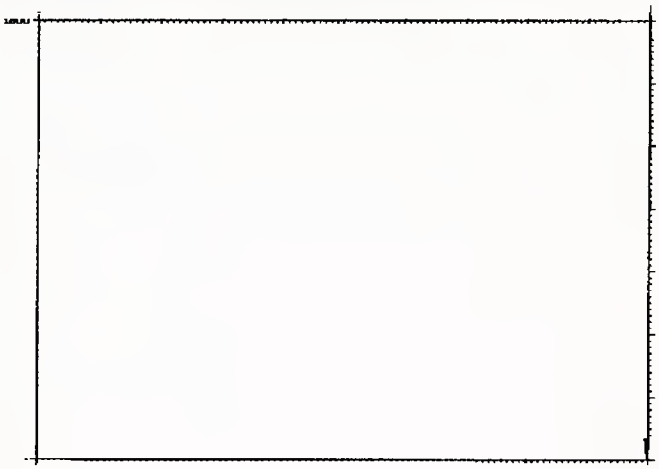

### 1.5.2 Crystal Structures

The lattice parameters of pure Au and Pt at 25°C are accepted as 0.40784nm and 0.39233nm. The Au-Pt system has only one stable structure (Au, Pt) based on the Cu-type fcc solid solution. The deviation from an assumed Vegard's law is very slight (Fig.1.18).

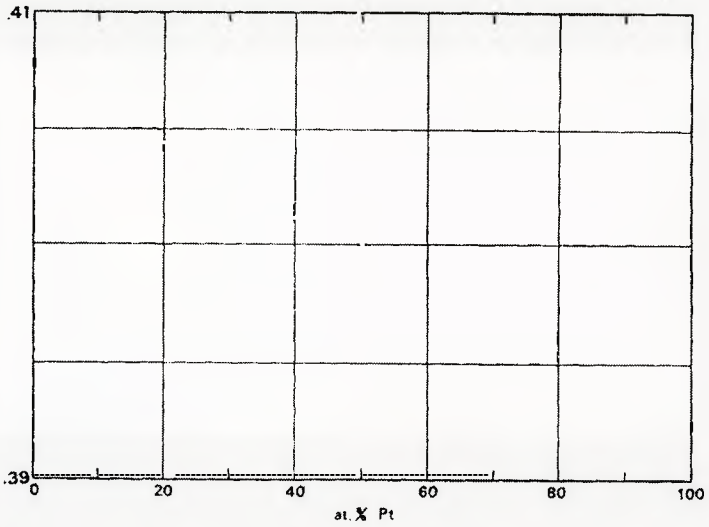


Fig. 1.18 Trend of lattice parameter with composition (at%Pt) in the Au-Pt system (Okamota and Massalski, 1985)

### 1.5.3 Thermodynamics

The thermodynamic functions of solid and liquid phases, on which Okamoto and Massalski based their model of the Au-Pt phase diagram (Fig.1.17), are listed in the Table1.1. They did mention that both liquidus and solidus functions would benefit from re-examination.

| | | |
|---|---|---|
| Lattice stability parameters (J/mol) | $G_L^0(Au)$ | 0 |
| | $G_L^0(Pt)$ | 0 |
| | $G_s^0(Au)$ | $-13000+9.7190T$ |
| | $G_s^0(Pt)$ | $-19650+9.6224T$ |
| Excess Gibbs free energy (J/mol) | $\Delta G_L^{ex}$ | $x(1-x)(23500+4000x)$ |
| | $\Delta G_s^{ex}$ | $x(1-x)[30000x-(-13.00+14.183x)T]$ |

Table1.1 thermodynamic functions for Au-Pt phase diagram (Okamota and Massalski,1985)

The expressions for Gibbs free energy, enthalpy, entropy and heat capacity of Au and Pt are evaluated by SGTE (Scientific Group Thermodata Europe) (Dinsdale, 1991). The pure Au and pure Pt transition data are listed in Table1.2.

| | | Atomic wt | $H_{298}$-$H_0$ | $S_{298}$ | $T_{trans}$ | $\Delta_{trans}H$ | $\Delta_{trans}S$ | $\Delta_{trans}Cp$ |
|---|---|---|---|---|---|---|---|---|
| Au | FCC_A1 | 196.9665 | 6016.592 | 47.4884 | 1337.33 | 12552 | 9.3859 | 0.0 |
| Pt | FCC_A1 | 195.08 | 5723.712 | 41.6308 | 2041.5 | 22175 | 10.8621 | -0.8317 |

**Table 1.2. SGTE pure element transition data (Dinsdale, 1991)**

# CHAPTER 2

# SYNTHESIS

Perepezko (2001) and Battezzati (1999) have successfully formed Al/Ni multilayers with layer thickness of 50nm by repeated cold rolling and folding. There are two main advantages of this process. One is that the process allows for retention of high purity; the other is that the sample remains at low temperature during process provided the deformation rates are low. Therefore, Au/Pt multilayers with layer thickness of 30nm have been formed based on Perepezko's experimental approach. However, non-uniform structure, including folded edges and delamination were observed by SEM and TEM. Yasuna and co-workers (1997) have formed regular and well-welded Fe/Ag multilayers with layer thickness as low as 10nm by a repeated cut-stack-anneal-press-anneal-rolling approach. Considering these facts, the experimental procedure was improved. In this section, two approaches of synthesis will be described. The experimental preparation and details of rolling/folding process will be given in section (2.1) and (2.2). The improved experimental procedure will be given in section (2.3).

## 2.1 Experimental Preparation

The materials, pack, rolling mill and measure tool needed for this work are as following:

(1) Pure Au and Pt foil (Alfa Aesar Company; Au purity 99.9975+%, Pt purity 99.998%);

(2) Pack (3-quarter hard stainless steel polished with sand paper);

(3) Manual rolling mill (cylinders length of the rolls 80mm, diameter of the rolls 54mm);

(4) Digital micrometer with resolution to $\pm 1\mu m$.

### 2.1.1 Prediction of Average Layer Thickness

Interfacial free energy and grain boundary energy are size-dependent, thus we need to predict average layer thickness for each rolling/folding (R&F) cycle. For ideal conditions, dividing the total layer thickness by the number of layers gives the average layer thickness. Therefore, assuming the total specimen thickness is 80μm after each R&F cycle, the average layer thickness is estimated after each cycle, as shown in the Table 2.1.

| No. of R&F | No. of layers | Average Layer thickness |
|---|---|---|
| 1 | 4 | 20μm |
| 2 | 8 | 10 μm |
| 3 | 16 | 5 μm |
| 4 | 32 | 2.5 μm |
| 5 | 64 | 1.25 μm |
| 6 | 128 | 625nm |
| 7 | 256 | 313nm |
| 8 | 512 | 156nm |
| 9 | 1024 | 78nm |
| 10 | 2048 | 39nm |
| 11 | 4096 | 20nm |
| 12 | 8192 | 10nm |
| 13 | 16384 | 5nm |
| 14 | 32768 | 2.5nm |

Table 2.1. Prediction of layer thickness after each cycle

## 2.2 Repeated Cold Rolling and Folding (R&F) Experiment

The pure Au and Pt foils ($20mm \times 10mm \times 80\mu m$) were folded three times to form a $5mm \times 5mm$ multilayer sandwich. The sample weight was typically about 0.5g. The sandwich was pack-rolled in one direction at room temperature in air to approximately 80μm for about 10 passes. A small piece of the sample ($20\mu g - 40\mu g$) was retained for examination. The rest was folded to double thickness and pack-rolled to around $80\mu m$. The cyclic operation was repeated up to 20 times. The pack was changed every two cycles. The final material was cold rolled up to 200 passes.

In chapter 3, the results of microstructural investigations using techniques of: X-ray diffraction (3.1), scanning electron microscopy (3.2) and transmission electron microscopy (3.3) are reported. For clarity, the techniques are discussed separately.

## 2.3 Repeated Cut-Stack-Anneal-Rolling Experiment

### 2.3.1. Experimental Design

Folded edges were clearly shown in the SEM images at low rolling and folding (R&F) cycles. Moreover, after the R&F process, the stack sequence of multilayers is Au-Pt-Pt-Au instead of Au-Pt-Au-Pt. Another important aspect is the welding ability of Au/Pt multilayers. Delaminations were observed even at high R&F cycles. Non-welding will cause two problems. Firstly, if we use cross-sectional TEM sample to analyze

microstructure, the microtomed samples may not be sufficiently representative. Secondly, delaminations would damage the interfaces between Au and Pt layers, which will influence the thermal stability. Although the folded edges and non-welding situations take place locally, the material is not considered satisfactory to further studies.

Yasuna and co-workers (1997) have successfully fabricated bulk Fe/Ag multilayers with layer thicknesses as low as 10nm by repeated cut-stack-press-anneal-rolling procedure. The multilayers are uniform, well-welded and have a nearly perfect orientation relationship to each other. Thus, rolling/folding procedure would be improved to get better multilayers. The two important criteria are discussed as following:

(1) Uniform Structure

Repeated cut-stack-rolling instead of rolling/folding avoids folded edges as well as the Au-Pt-Pt-Au stacking sequence.

(2) Welding Ability and Layer Thickness

Two possible reasons cause locally non-welding conditions. Firstly, oil and dirt left on the sample during processing could inhibit welding. The oil might be a trace of machine oil, or derived from handling. Secondly, work hardening is induced by the plastic deformation. Yasuna (1997) proposed that preliminary annealing would weld layers and annealing during each cycle would remove defects and strain. But, he also put

forward that the limit of reduction of layer thickness may be attributed to the heat treatment prior to the rolling process.

Given the considerations above, the following improvements were made: First, a cleaning step was added after each rolling cycle. The sample was cleaned in a bath type sonicator with the sequence 10%Nitric Acid-Water-Acetone-Ethanol for ten minutes to remove oil and dirt. Second, pure Au and Pt foils were annealed at $900^{\circ}C$ to obtain preliminary joining of the layers. However, the annealing temperature during each rolling cycle was reduced to $250^{\circ}C$ until a layer thickness of about 10nm was attained. Thereafter, the sample was cold rolled (without annealing during rolling cycle) until theoretical layer thickness of approximately 2.5nm was reached.

### 2.2.2 Experimental Details

A schematic illustration of experimental procedure was shown in Fig.2.1. The experimental details are shown below:

(a) One piece of pure Au and Pt foils ($20mm \times 15mm \times 90\mu m$) were stacked together and pack-rolled in one direction at room temperature in air to approximately $90\mu m$ for about 10 passes. The sample was cut into two identical pieces, and cleaned in a bath type sonicator with the sequence 10%Nitric Acid-Water-

Acetone-Ethanol, each for 10 minutes. Then, samples were annealed in the quartz tube furnace at $900^{\circ}C$ for 16 hours in vacuum.

(b) The two pieces were stacked together and pack-rolled to $80\mu m - 90\mu m$ for about 10 passes. A small piece of the sample $(20\mu g - 40\mu g)$ was retained for examination. The rest was cut and cleaned. The two pieces were annealed at $250^{\circ}C$ for 16 hours in vacuum.

The cut-stack-rolling cycles were repeated for 14 times. But annealing time was reduced to 1 hour after 4 cycles. The samples were cold rolled without annealing after 12 cycles. The pack was changed every 2 cycles. The sample has small cracks at the edges after 7 times of cyclic operation. The cracks were trimmed and retained.

The microstructure will be characterized by XRD and TEM. We will discuss the results in chapter 4.

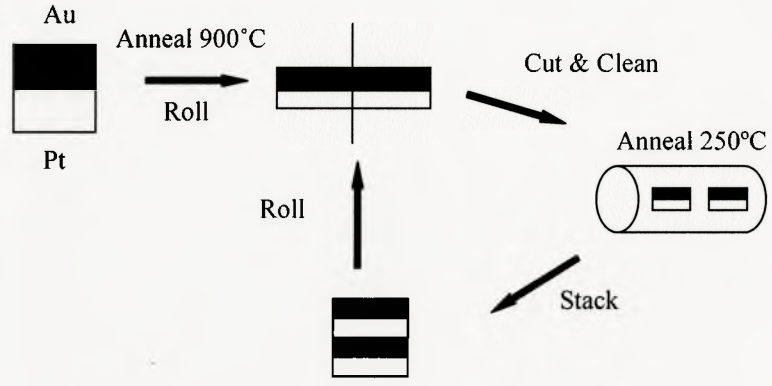


Fig.2.1 Schematic illustration of repeated cut-stack-anneal-rolling procedure. After 12 cycles, the samples are cold rolled (without annealing) to 14 cycles.

# CHAPTER 3

# CHARACTERIZATION OF MULTILAYERS FORMED BY ROLLING AND FOLDING

In this chapter, X-ray Diffraction, Scanning Electron Microscopy and Transmission Electron Microscopy will be used to characterize the microstructure of Au/Pt multilayers formed by rolling/folding process. The process formed Au/Pt multilayers with layer thicknesses of approximately 30nm and did not induce the formation of solid solution. Non-uniform structure and non-welding situation were observed locally. These may be caused by limitations of the process.

## 3.1. X-Ray Diffraction (XRD)

XRD analysis was conducted using a Nicolet I2 X-ray powder diffractometer and $CuK_{\alpha}$ radiation with a wavelength of 1.54Å.

The phases and grain size of the samples formed by rolling/folding after 30passes and 200passes were characterized by XRD, shown in Fig.3.1. XRD patterns show only elements reflections after rolling. With increasing number of rolling passes, the peak heights decrease, and the peaks broaden due to decreasing grain size. The average grain size is 30nm after 200passes.

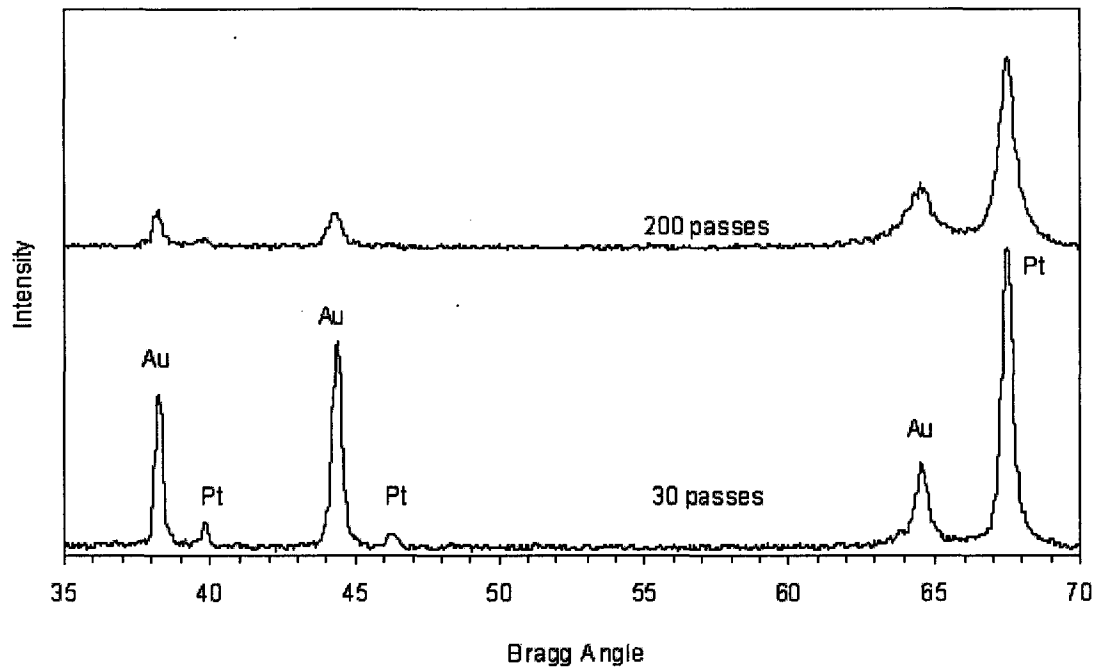


Fig.3.1 XRD scan of the rolling/folding multilayers after 30 and 200passes. The peak heights decrease and the peaks broaden due to decreasing grain size. The average layer thickness is approximately 30nm after 200passes.

### 3.2. Scanning Electron Microscopy (SEM)

Philips SEM 515 with a Link Analytical Pentafet X-ray microanalyzer was used to characterize the multilayer morphology after low rolling passes.

#### 3.2.1 Cross-sectional Specimen Preparation

The procedure of cross-sectional SEM sample preparation is listed as below.

(a) The sample (5mg) was held by a plastic clip, and placed into a solution consisting of 1.5 parts resin and 2.2 parts harder for overnight at room temperature.

(b) The mounted specimen was ground with wet silicon carbon paper.

(c) Polishing discs were covered with soft cloth impregnated with abrasive diamond particles and oil lubricant. After 3 stages (6μm, 3μm, 1μm) of polishing, the specimen was final polished with a 200ml colloidal silica solution.

(d) The surface of the specimen was painted with conductive silver-gold.

### 3.2.2 SEM Results and Discussion

(1) Structure Evolution

The cross-sectional SEM images in Fig.3.2 show the microstructure of different areas of the multilayers, which were formed by repeated rolling/folding after 40passes. Darker layers were identified as Pt, and brighter ones as Au by means of the energy dispersive X-ray analysis (EDX). Au is softer than Pt. After a few rolling passes, the Pt foils appeared broken in fragments which were dispersed in the Au matrix. Pt particles are aligned along the rolling direction. Some have filamentary ends, and their surfaces display a wavy appearance. Bulging and serrations were observed from Fig3.2. With further rolling, the layers became more and more refined, and the thickness of each layer became more uniform. This process eventually yielded a relatively homogeneous multilayer pattern after 50-60 rolling passes.

Fig 3.2 SEM/BSE (backscattered electron) cross-sectional images of different areas of Au/Pt multilayers after rolling/folding 40 passes

(2) Folded Edges and Welding Ability

Folded edges can be seen clearly in Fig.3.3. It would cause non-uniform distribution of the layer thickness. Fig3.3 also shows delamination of multilayers.

Fig.3.3 SEM/BSE (backscattered electron) cross-sectional image of Au/Pt multilayers after rolling/folding 60passes. Folded edges and delamination of layers are observed.

## 3.3 Transmission Electron Microscopy (TEM)

### 3.3.1 Cross-sectional TEM Sample Preparation

The procedure of specimen preparation is listed as below. The schematic illustration of cross-sectional TEM sample is shown in Fig.3.4. Plastic film, inserted between multilayers and Cu grid, is used to support multilayers.

(a) The sample was cleaned using acetone in a bath type sonictor for about half an hour at room temperature.

(b) The sample was then placed into 100% Spurr's epoxy resin (three changes over two days at room temperature).

(c) The sample was hardened overnight in an oven at 65°C~70°C.

(d) The sample was cut on helical ultra cut, and put on 200mesh copper or palladium grids.

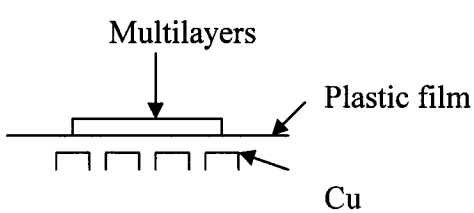


Fig.3.4 Schematic illustration of cross-sectional TEM sample

### 3.3.2 TEM Results

The well-prepared TEM samples were viewed with Philips CM12 TEM.

Fig.3.5 shows cross-sectional TEM bright field images for Au/Pt multilayers prepared by the repeated rolling/folding after 200passes. Fig3.5 (a) low magnification image shows that the repeated rolling/folding procedure has successfully resulted in an Au/Pt multilayer. The multilayers had wavy structures and they developed a plastic flow pattern. Fig3.5 (b) shows that the regular multilayers are parallel to each other along rolling direction, and that the average layer thickness is around 30nm. It is difficult to distinguish Au from Pt in the image. Band structures were observed cross the grains due to severe deformation.

Fig3.6 shows cross-sectional TEM bright field images for Au/Pt multilayers prepared by the repeated rolling/folding after 110passes. Well-welded and regular lamellae were observed locally. The average layer thickness is in the range of 60-70nm. We are interested in knowing whether the regular lamellae have a consistent orientation relationship. Thus, diffraction patterns of the two paralleled layers and interface were studied. However, a consistent orientation relationship has not been observed.

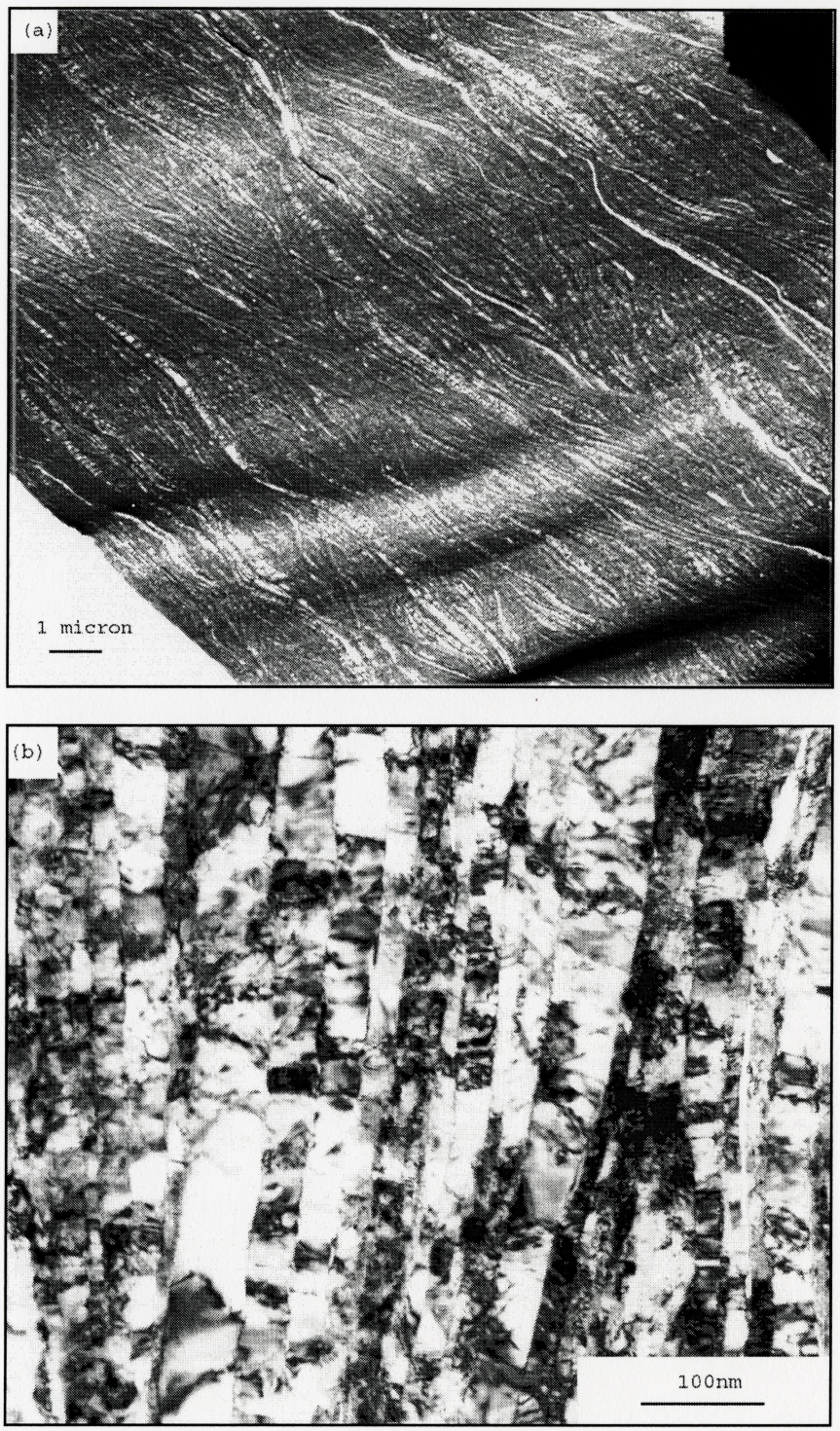


Fig3.5 Cross-sectional TEM bright field images for Au/Pt multilayers prepared by the repeated rolling/folding after 200passes: (a) lower magnification image (b) higher magnification image. Regular Au/Pt multilayers have been formed by rolling/folding process.


Fig.3.6 Cross-sectional TEM bright field images for Au/Pt multilayers prepared by the repeated rolling/folding after 110passes. Regular multilayers are observed locally.

# CHAPTER 4

# CHARACTERIZATION AND THERMAL STABILTIY OF MULTILAYERS FORMED BY CUT-STACK-ROLLING

Characterization by XRD and TEM shows that relatively uniform and well-welded multilayer structure has been formed by repeated cut-stack-rolling process. The average grain size is 6nm after 14 cycles. The most important result is that the Au-50%Pt solid solution formed at room temperature. Moreover, the 50/50 solid solution is rather unstable, it decomposes into Au and Pt after DSC heating to 500°C at 50°C/min. The XRD and TEM results will be given in section (4.1) and (4.2) respectively. In section (4.3), DSC annealing results will be presented. The driving force, mechanism and thermal stability of the 50/50 solid solution will be discussed in section (4.4).

## 4.1 X-ray Diffraction

The phases and grain size of the sample formed after 14 rolling cycles were characterized by XRD.

### 4.1.1 Solid Solution Formation

Solid solution peak was detected by Nicolet I2 X-ray powder diffractometer with $CuK_{\alpha}$ radiation. The result was confirmed by high resolution D8 Advanced X-ray diffraction with $CuK_{\alpha 1}$ radiation. The resolution of D8 Advance is 0.05 degree while that

of Nicolet I2 is 0.2 degree. The high-resolution XRD curve in wide range angle is given in Fig.4.1. Au and Pt peaks are listed in Table 4.1. Fig 4.1 clearly demonstrates that there is a centre peak between Au (220) and Pt (220) reflection. The centre peak is identified as a solid solution. The shape and position of the three peaks at (220) reflection were modeled with Origin6.0 software, provided each peak fits Gaussian distribution (Fig.4.2). The strong solid curve is the overlap of the three peaks, which fits the experimental data well. In Fig4.2, it clearly illustrated a solid solution peak in the overlap region of the broadening Au and Pt peaks. The intensity of solid solution peak is much lower than that of Au and Pt peaks. It indicates that only small amount of solid solution was formed during rolling. The lattice parameter of the solid solution is approximately 0.40nm. According to the Vegard's law, it is Au-50%Pt solid solution. The detailed solution of determination of lattice parameters is given in Appendix1. In addition, Fig.4.2 also demonstrates strong deformation texture.

| hkl | 2θ (Degree) | |
|---|---|---|
| | Au Peaks | Pt Peaks |
| 111 | 38.184 | 39.763 |
| 200 | 44.392 | 46.243 |
| 220 | 64.576 | 67.454 |

**Table 4.1 Structure parameters of pure Au and pure Pt**

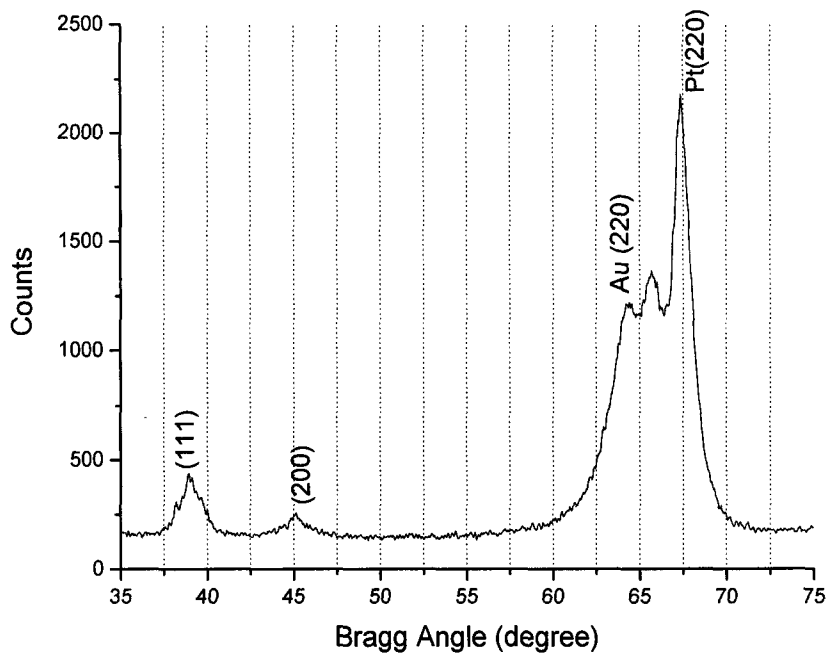


Fig.4.1 XRD scan of Au-50%Pt multilayers formed by repeated cut-rolling after 14 cycles. Au-50%Pt solid solution reflection was detected.

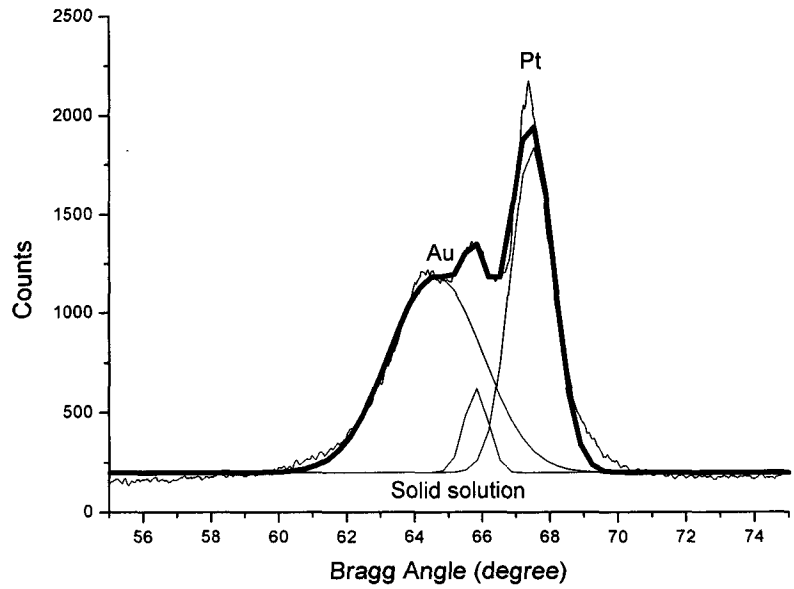


Fig.4.2 Simulation of Au, Pt and solid solution peaks. A small solid solution peak is in the overlap region of broadening Au and Pt peaks.

### 4.1.2 Grain Size Measurement

The Scherrer formula is used to estimate small grain size from measured full-width at half maximum (FWHM) in the diffraction curve. After taking into account instrument broadening correction term, the grain size is found to be approximately 6nm. The result neglected inhomogeneous microstrain resulting from mechanical deformation. The solution is given in Appendix 2.

## 4.2 Transmission Electron Microscopy

The cross-sectional TEM samples (after 11, 12 and 14 cycles) were viewed with Philips CM12 TEM.

### 4.2.1 Well-welded and Uniform Multilayers

Figure 4.3 shows bright field TEM images of cross-sectional sample after 11 cut-rolling cycles. Fig.4.3(a) shows that the improved process has successfully formed well-welded lamellae. In Fig.4.3(b) and Fig.4.3(c), high magnification images show a rather regular multilayer structure with the layer thicknesses ranging 20-30nm. Grains of various shapes embedded in layers and dislocation walls formed locally along interfaces.

Fig.4.4 shows bright field TEM images of cross-sectional sample after 12 cut-rolling cycles. In Fig.4.4(c), the average layer thickness is around 10nm. Compared with Fig.4.3, we can see the grain size is much smaller and more uniform. Another interesting

point is that most of small grains represent cubic shape. It implies that dynamic recrystalization takes place during severe deformation.

### 4.2.2 Solid Solution Formation

High-resolution XRD strongly demonstrates the 50/50 solid solution formation during 14 cut-rolling cycles. Thus, it is very interesting to know *where* the solid solution forms. The dark-field TEM image and diffraction pattern of Au-50%Pt multilayers after 14 cut-rolling cycles are shown in Fig.4.5. It clearly demonstrates that the bright phase is 50/50 solid solution reflection and dark layers are Au and Pt (To correct the angle rotation of image with respect to diffraction pattern, the image should be rotated 12° clockwise). Multilayers are discontinuous homogenized along the rolling direction.

The average layer thickness of this image is 6nm. The TEM result of grain size measurement is consistent with the result of XRD.

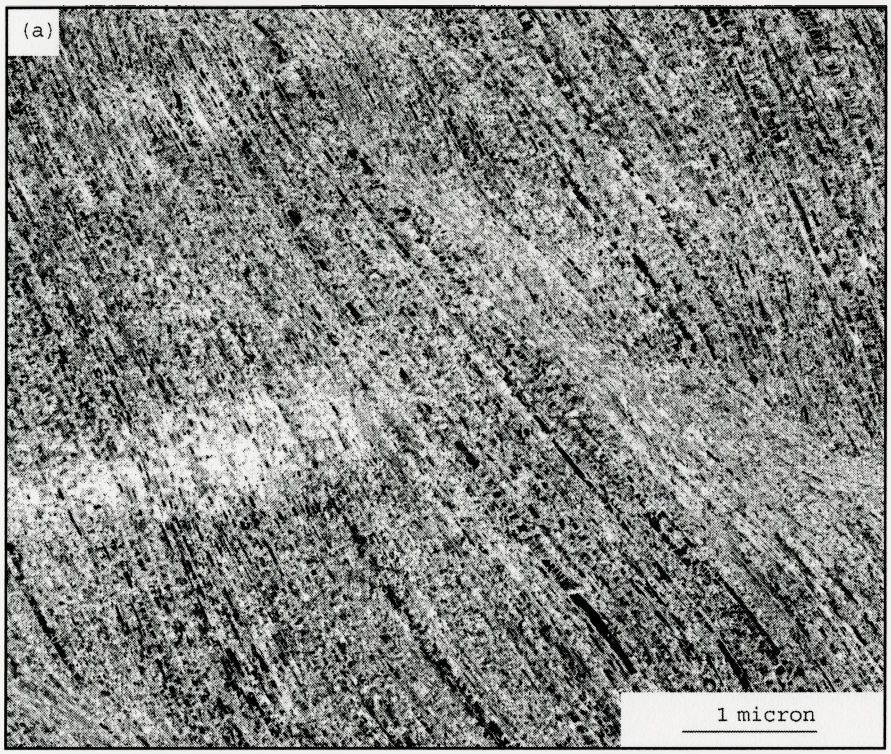
(a)
1 micron

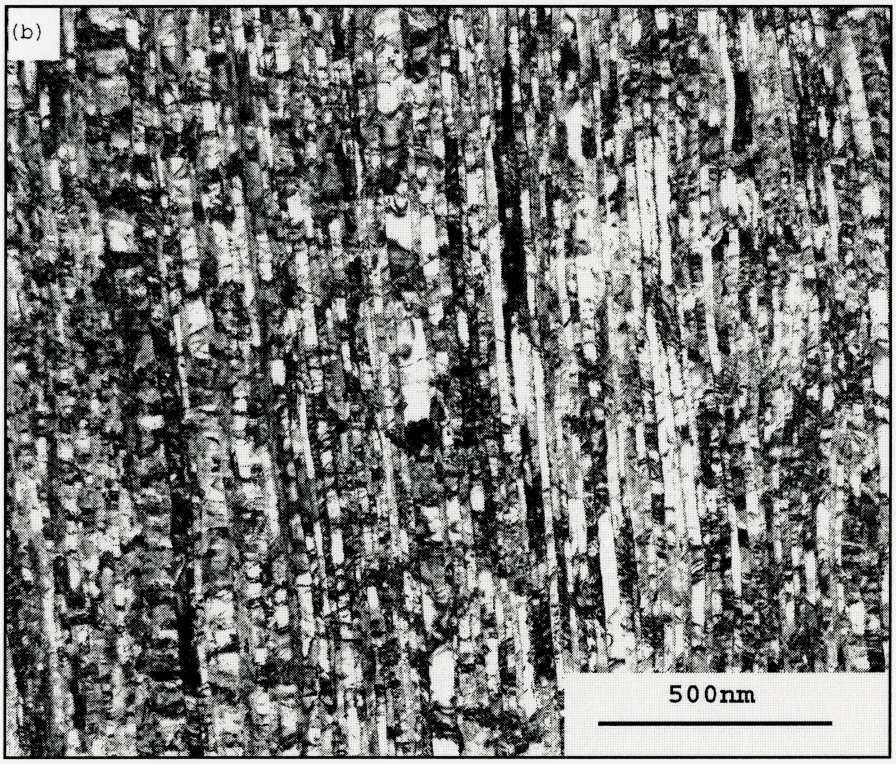
(b)
500nm

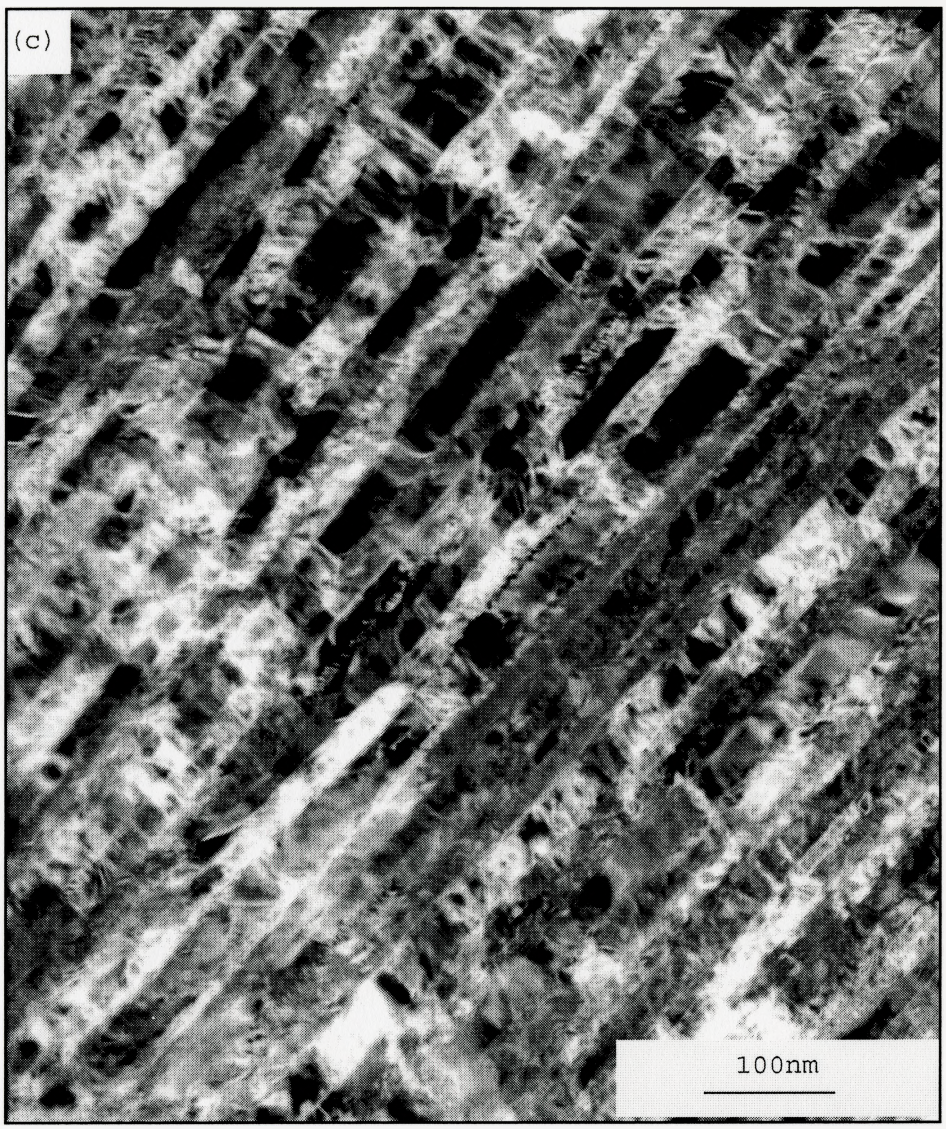


Fig.4.3 Cross-sectional TEM bright field images for Au/Pt multilayers prepared by the repeated cut-rolling procedure after 11 cycles: (a) low magnification image (b) medium magnification image (c) high magnification image. Well-welded and uniform multilayers have been formed by the process. The average layer thickness after 11 cut-rolling cycles is 20-30nm.

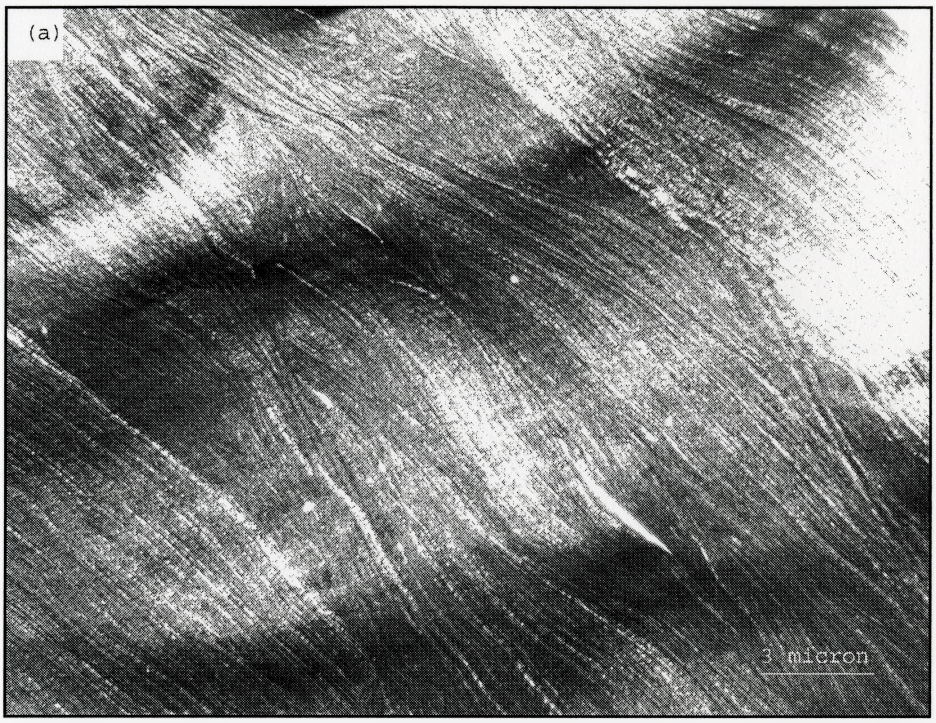
(a)
3 micron

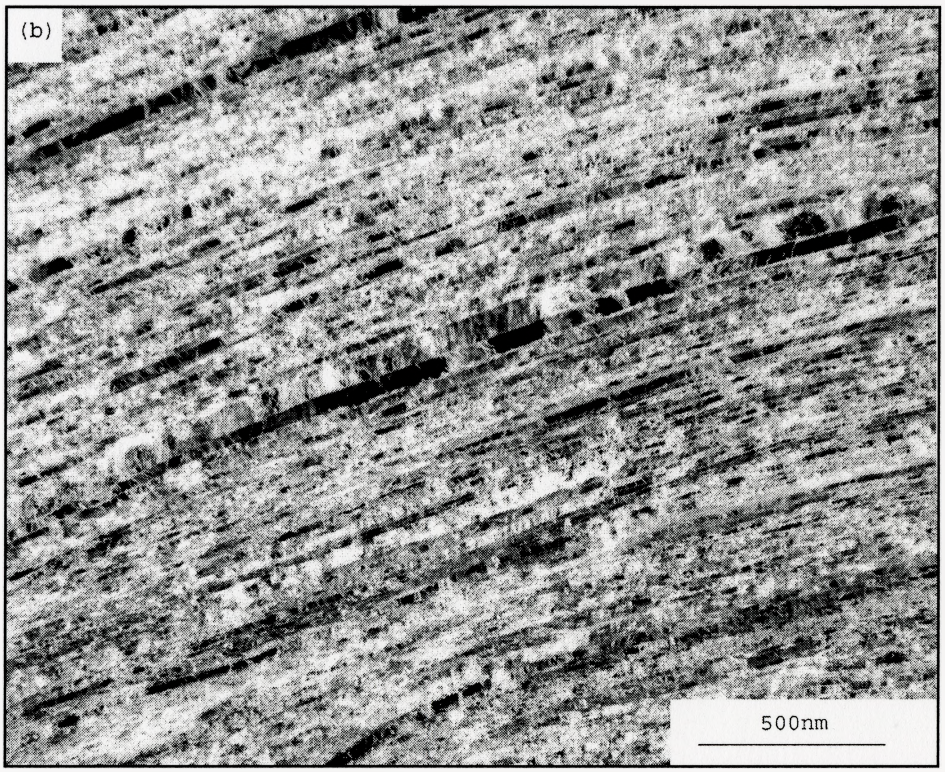
(b)
500nm

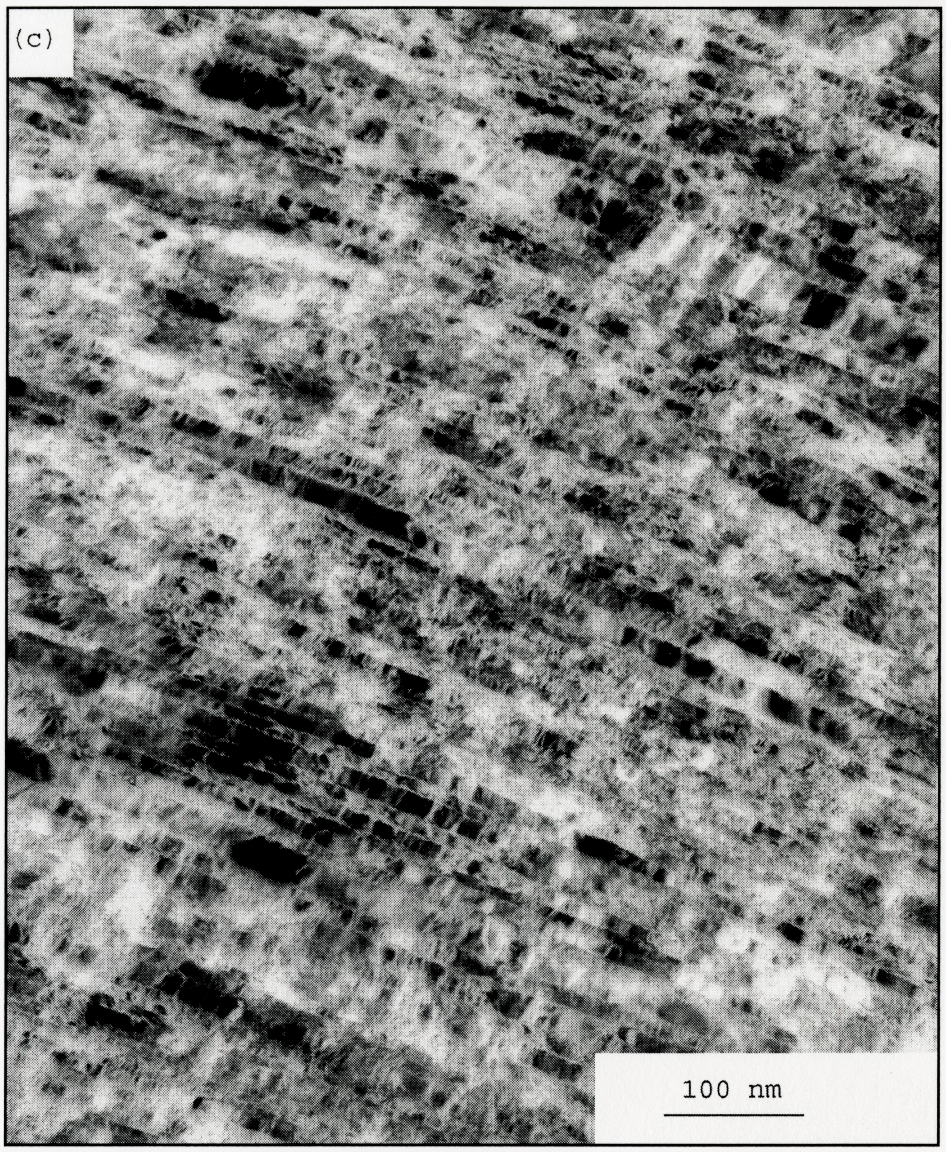


Fig.4.4 Cross-sectional TEM bright field images for Au/Pt multilayers prepared by the repeated cut-rolling procedure after 12 cycles: (a) low magnification image (b) medium magnification image (c) high magnification image. The average layer thickness after 12 cut-rolling cycles is approximately 10nm.

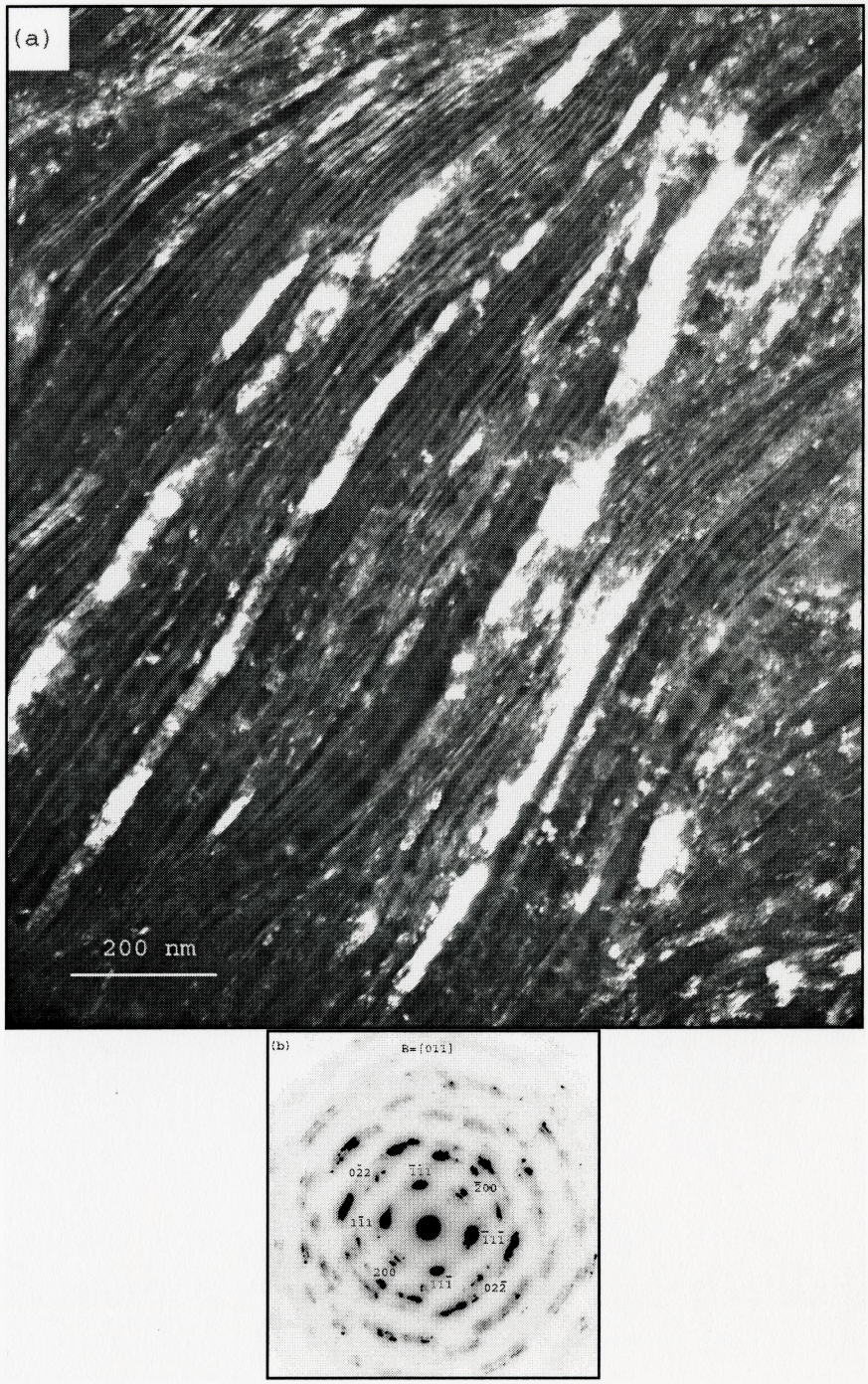


Fig.4.5 Cross-sectional TEM images and diffraction pattern of Au/Pt multilayers after 14 cut-rolling cycles: (a) dark-field image, the bright phase is 50/50 solid solution and dark layers are Au and Pt (b) diffraction pattern.

## 4.3 Annealing Experiments

### 4.3.1 Experimental Details

To study the thermal stability of Au/Pt multilayers, a low temperature heat treatment was carried out by Differential Scanning Calorimetry (DSC). The fastest heating rate was employed to prevent coarsening of fine lamellae. The experimental details are as following.

The Au/Pt multilayers (6.5mg) after 14 cut-rolling cycles were cleaned with acetone. Then, the sample was put into pure Al pan and covered by Al cover, and annealed by DSC from room temperature to 500°C at heating rate 50°C/min under argon. At last, the sample was cooled to room temperature with ice. The microstructure of the annealed sample was characterized by XRD and TEM.

### 4.3.2 Experimental Results

#### 4.3.2.1 X-ray Diffraction (XRD)

XRD was conducted with Nicolet I2 X-ray powder diffractometer with $CuK_{\alpha}$ radiation at high angle range. Fig.4.6(a) is the XRD curve of cut-rolling sample before annealing, while Fig.4.6(b) is the curve of the same sample after annealing. Comparing

Fig.4.6(a) with Fig.4.6(b), we found that the solid solution peak disappeared after annealing. Au and Pt peaks shift compared to position of pure Au and pure Pt peaks. Lattice parameter of (Au) solid solution is approximately 0.4042nm. According to Vegard's Law, there is about 80% Au in the solid solution (Appendix 1). Thus, the 50/50 solid solution decomposed to (Au) and (Pt) solid solutions after DSC heating to 500°C at 50°C/min.

#### 4.3.2.2 Transmission Electron Microscopy (TEM)

The microstructure of annealed sample was examined using the Philips CM12 TEM. The cross-sectional TEM sample preparation is exactly the same as mentioned in chapter 3. Fig.4.7 is the bright field image of Au-Pt multilayers subjected to cut-rolling after 14 cycles and DSC heating to 500°C at 50°C/min. Microstructural changes are clearly observed from Fig.4.7.

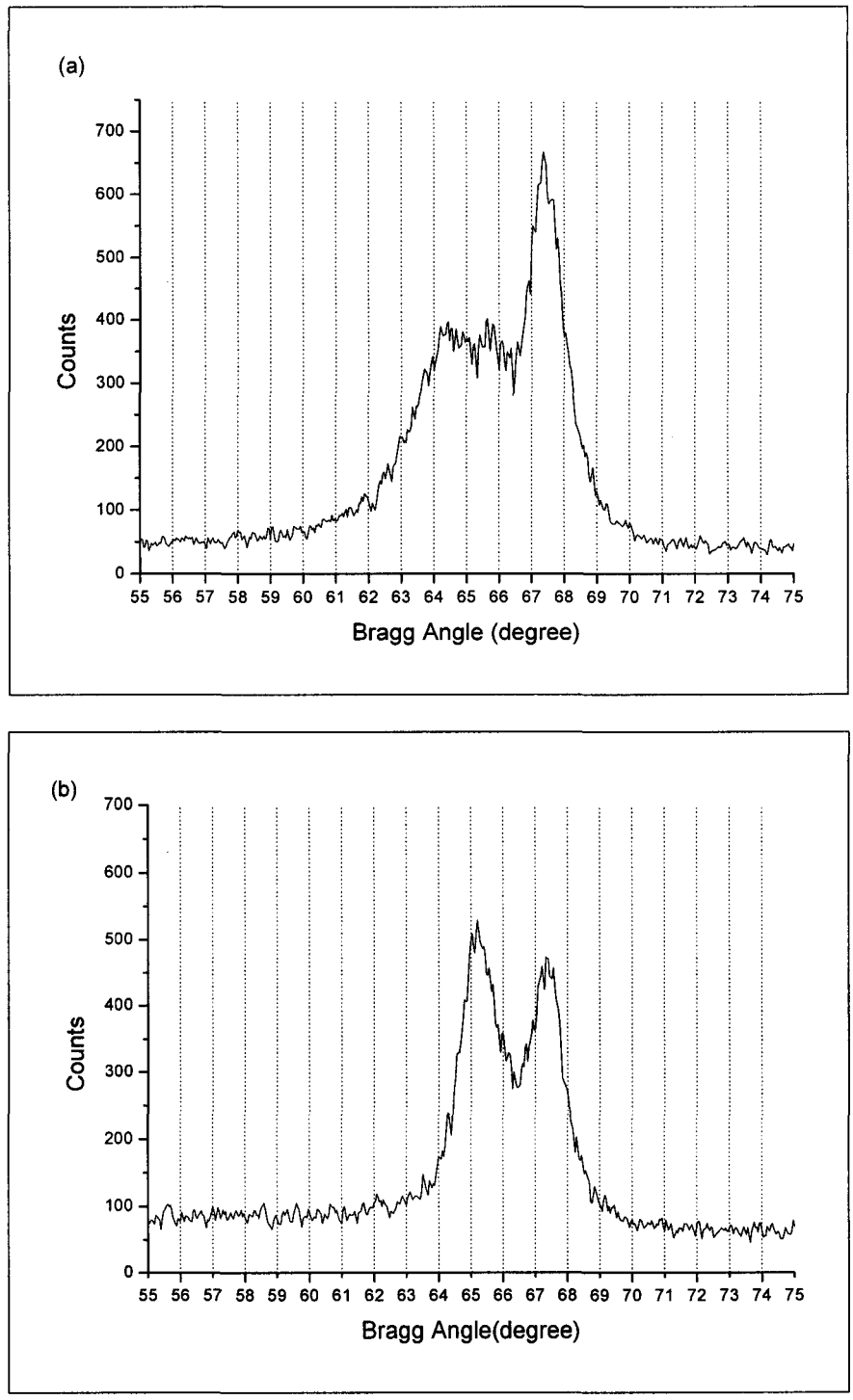


Fig.4.6 XRD curves of Au/Pt multilayers subjected to 14 cut-rolling cycles with/without DSC heating to 500°C at 50°C/min: (a) before annealing (b) after annealing. The 50/50 solid solution decomposes into (Au) and (Pt) solid solutions after low temperature heat treatment.

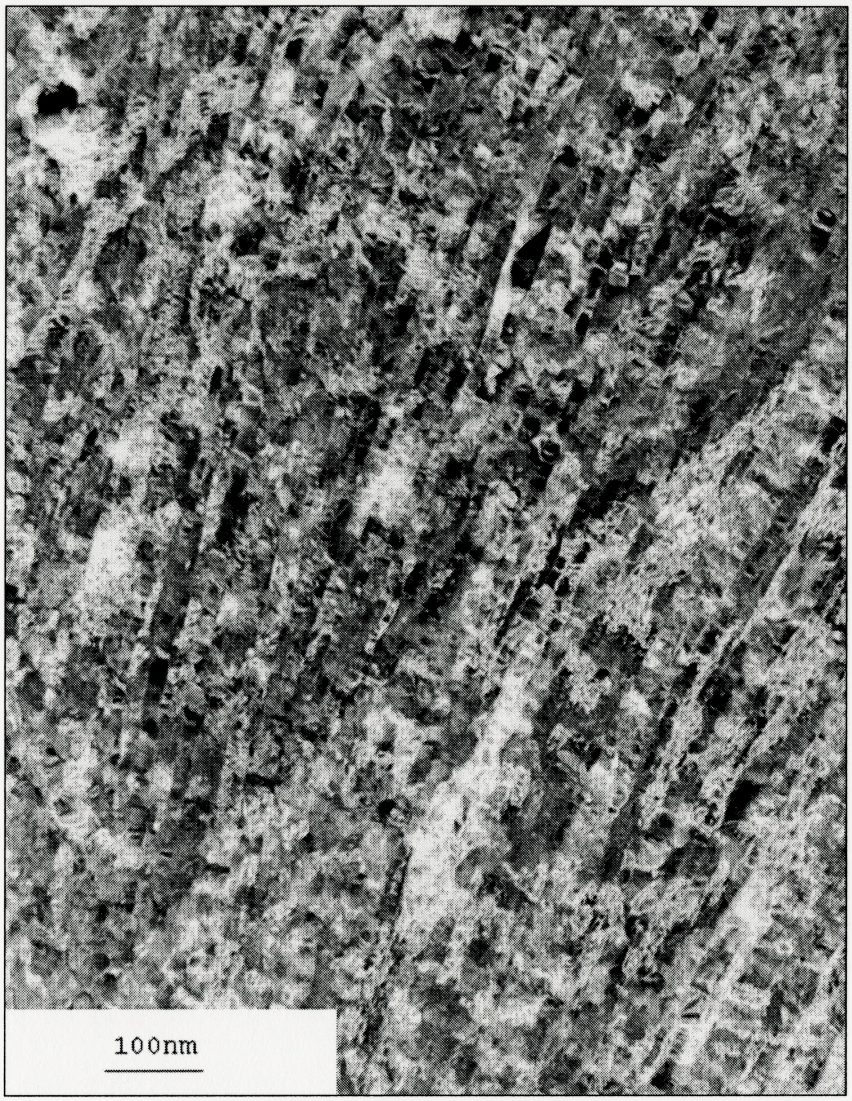


Fig.4.7 Cross-sectional TEM bright field image of Au-Pt multilayers subjected to cut-rolling 14 cycles and DSC heating to 500°C at 50°C/min.

## 4.4 Discussion

### 4.4.1 The Driving Force of the Formation of Solid Solution at 298K

It is at first surprising that an Au-50%Pt solid solution can form during cold rolling at room temperature. The reason may lie in the fact that the interfacial free energy and grain boundary energy stored in the system are higher than the barrier to form solid solution. The free energy barrier to solid solution formation, as well as the magnitudes of interfacial free energy and grain boundary energy at 298K will be discussed in the following sections.

#### 4.4.1.1 Energy barrier to form solid solution at 298K

Figure 4.8 demonstrates how the barrier height is calculated. The curve is the Gibbs energy of solid solution for Au-Pt system at 298K. The line represents the stable common tangent in the miscibility gap for f.c.c. phase when the composition varies between approximately 0.0718 and 0.9999 mole fraction of Pt. At 298K, the driving force $\Delta G$ to form 50/50 solid solution is thus the shortest distance between the curve and the equilibrium common tangent line, as marked in the diagram. The numerical estimate of $\Delta G$ (Appendix 3), indicates that $\Delta G$ is of order 2600 J/mol.

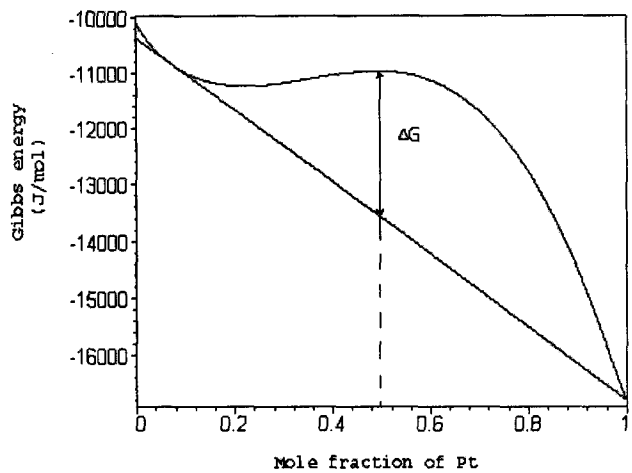


Fig.4.8. Definition of energy barrier to form 50/50 solid solution at 298K:
The curve illustrates the Gibbs energy of solid solution for Au-Pt system. The line represents the stable common tangent in the miscibility gap. ΔG is the driving force required for the formation of 50/50 solid solution.

### 4.4.1.2 The Interfacial Free Energy and Grain Boundary Energy

The total change in the Gibbs free energy of multilayers, neglecting stain energy, can be divided into two parts: interfacial free energy and grain boundary energy. In order to estimate these energies, we first present a simple model: A regular periodic multilayer composed of alternated layers of pure Au and Pt, as suggested by Fig.4.9. We assume that the system is free of elastic strains, and the layers are of equal thickness. Each grain is cubic and has perfect cube/cube orientation relationship.

Fig.4.9 Schematic model of Au-Pt multilayers: A regular periodic multilayer composes of alternated layers of pure Au and Pt, We assume that the system is free of elastic strains, and the layers are of equal thickness. Each grain is cubic and has perfect cube/cube orientation relationship.

(1) Grain Boundary Energy:

The grain boundary energy can be written as

$$\Delta G_b = \Delta G_{bAu} + \Delta G_{bPt} \tag{4.1}$$

where $\Delta G_{bAu}$ and $\Delta G_{bPt}$ are the grain boundary energies of Au and Pt respectively. $\Delta G_{bAu}$ is given by

$$\Delta G_{bAu} = \gamma_{Au} \times (2a^2) \times N \tag{4.2}$$

where $\gamma_{Au}$ is the grain boundary energy of Au per unit area. $2a^2$ is grain boundary area of per grain. $N$ is the number of Au/Pt grains in one mole Au-Pt multilayers. The $\Delta G_{bPt}$ can be calculated in the same way as $\Delta G_{bAu}$.

Thus, the grain boundary energy can be expressed as:

$$\Delta G_b = 2a^2 N(\gamma_{Au} + \gamma_{Pt}) \tag{4.3}$$

$\gamma_{Au}$ and $\gamma_{Pt}$ depend on temperature. Murr (1975), Butter (1953), Mclean and Honddros (1971) presented the values of grain boundaries of Au and Pt in Table 4.2.

(2) Interfacial Free Energy

The interfacial free energy is the integral of the sum of two contributions: one is incoherent free energy, estimated by average grain boundary energies of Au and Pt; the other is coherent interfacial free energy, a term that can be evaluated according to Cahn (1958).

$$\sigma = 2N_v \int_{c_\alpha}^{c_\beta} [\kappa \Delta f(c)]^{\frac{1}{2}} dc \tag{4.4}$$

where $N_v$ is the number of molecules per unit volume, $c_\beta$ and $c_\alpha$ are equilibrium compositions, $\kappa$ is gradient energy coefficient, $c$ is mole fraction of Pt component, $\Delta f(c)$ is the free energy per molecule referred to a standard state of an equilibrium mixture.

$\sigma$ depends on temperature. Computed values of $\sigma$ at different temperature are shown in Table 4.2. The solution is given in Appendix 4.

Therefore, the interfacial free energy is given by

$$\Delta G_\sigma = [\sigma + 0.5(\gamma_{Au} + \gamma_{Pt})] \times a^2 \times 2N \tag{4.5}$$

where $a^2 \times 2N$ is the total interface area.

Combining equations (4.3) and (4.5), we get the total change of Gibbs free energy

$$\Delta G = a^2 N[3(\gamma_{Au} + \gamma_{Pt}) + 2\sigma] \tag{4.6}$$

The change of Gibbs free energy of multilayers with grain size at different temperatures is shown in Fig.4.10. The detailed solution is given in Appendix 5.

| T (°C) | Grain boundary energy of Au $\gamma_{Au}$ ±14% (erg cm$^{-2}$) | Grain boundary energy of Pt $\gamma_{Pt}$ ±7% (erg cm$^{-2}$) | Coherent interfacial free energy (erg cm$^{-2}$) |
|---|---|---|---|
| 25 | 475.5 | 890 | 180 |
| 250 | 453 | 849 | 146 |
| 500 | 428 | 804 | 105 |
| 750 | 403 | 759 | 64 |
| 1000 | 378 | 714 | 26 |
| 1200 | 358 | 678 | 3 |

Table 4.2 Grain boundary energies of Au and Pt and coherent interfacial free energies of Au/Pt as a function of temperature. Values of grain boundary energy are selected from literature (Murr,1975, Butter, 1953, Mclean and Honddros, 1971). Values of coherent interfacial free energy are assigned by Maple software.

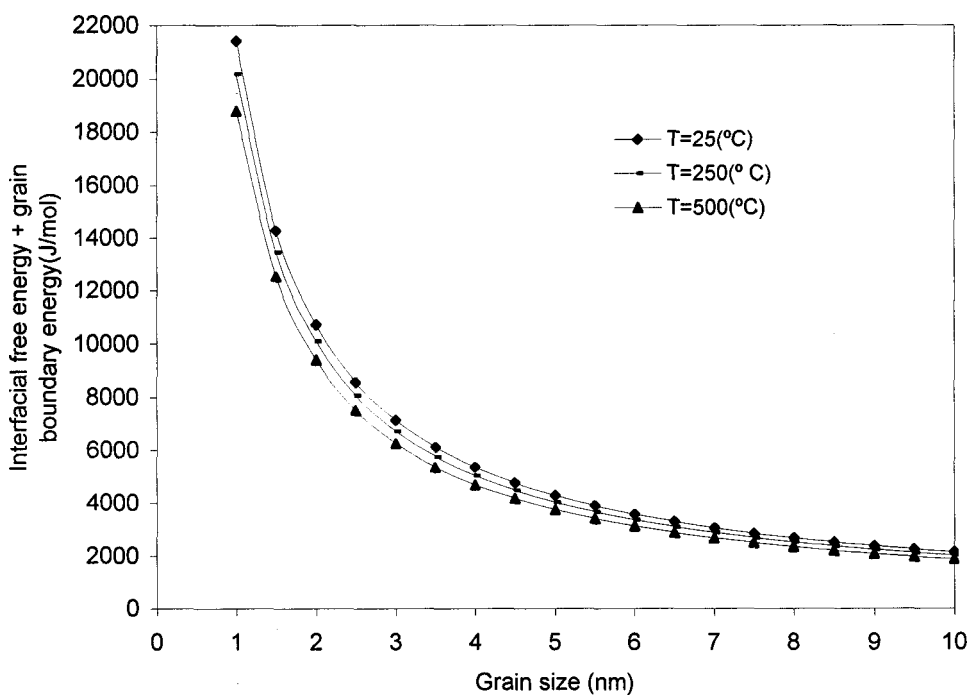


Fig.4.10 Interfacial free energy and grain boundary energy as a function of grain size at different temperatures.

At 298K, the total change of Gibbs free energy of multilayers with grain size 6nm $\Delta G$ is of order 3500J/mol. Compared to the barrier to form 50/50 solid solution, the total interfacial free energy and grain boundary energy are higher than the energy barrier. Thus, the 50/50 solid solution can form at room temperature. It is expected that the decomposition process occurs in the presence of plastic deformation; no further decomposition occurs when the samples are held at room temperature. Thus, interfacial diffusion is considered to be aided by defects generated during deformation.

### 4.4.2 Mechanism

Klinger, Brechet and Purdy (1997) proposed three different possibilities for the discontinuous homogenization of a monophase multilayer containing a mobile grain boundary: (a) the steady state motion of the boundary; (b) initially sinusoidal instability of the grain boundary; (c) the "fingering" instability of the moving boundary.

Among the three different possibilities, the steady state motion of the boundary adopts a constant, predictable velocity and shape. Compared with the TEM image Fig.4.5, the 50/50 solid solution appears a flat or near flat interface. Therefore, the steady state motion of the boundary is most likely expectation in the present studies.

### 4.4.3 Thermal Stability of 50/50 Solid Solution

Combining XRD and TEM results, we can attain that the solid solution Au-50%Pt is rather unstable. It decomposes to (Au) and (Pt) solid solutions after low temperature heat treatment. The process of decomposition is not understood. It is open to further theoretical and experimental investigations.

# CHAPTER 5

# PHASE EQUILIBRIUM

The bulk (Au-Pt) phase diagram is strongly modified at the nanometer scale because of the contribution of interface energy. For grain size approximately 10nm, there is a large shift of transition temperature. Melting temperature of Au/Pt multilayers is studied with theoretical and experimental approaches. A lowered melting point of multilayers is obtained with both approaches.

## 5.1 Grain-size Dependent Phase Diagram Model

Size driven phase transitions have not been widely studied. However, it can be expected that modification of the phase equilibrium diagram may be observed in nanoscaled grain sizes. In this work, we consider the Au-Pt multilayers with average grain size 10nm. Simplified assumptions and constructions of the phase diagram model will be presented first, then the results and discussion.

### 5.1.1 Assumptions and Construction

The surface energy varies with grain size and shape. In this model, we assumed that average grain size is 10nm. Each grain is cubic and has perfect cube/cube orientation relationship. Additionally, the system is free of elastic strains.

The phase diagram can be derived from the free energy curves for the solid and liquid phases. The surface energy is added into the Gibbs free energy of solid phase. Okmoto and Massalski (1985) presented thermodynamic functions for the liquid and solid phases of Au-Pt system. The Gibbs free energies of molar liquid and solid phases can be written as:

$$G_l = 8.314T[x\ln x + (1-x)\ln(1-x)] + x(1-x)(23500 + 4000x) \tag{5.1}$$

$$G_s = (-13000 + 9.7190T)(1-x) + (-19650 + 9.6224T)x + 8.314T[x\ln x + (1-x)\ln(1-x)] + x(1-x)[30000x - (-13 + 14.183x)T] \tag{5.2}$$

The equilibrium compositions at different temperatures are calculated by Maple software using common tangent line method. The detailed solution of peritectic temperature is in Appendix 6.

### 5.1.2 Results

The phase diagram model is shown in Fig.6.1. The light solid line represents the phase diagram of bulk materials, and the strong solid line stands for the phase diagram model with grain size 10nm.

The present phase diagram model shows the large shift of transition temperature. Fig.5.1 reveals that the melting temperatures of Au and Pt can be lowered more than 300K. The lens-shaped solidus-liquidus curves are shifted to lower temperatures and a peritectic reaction may occur.

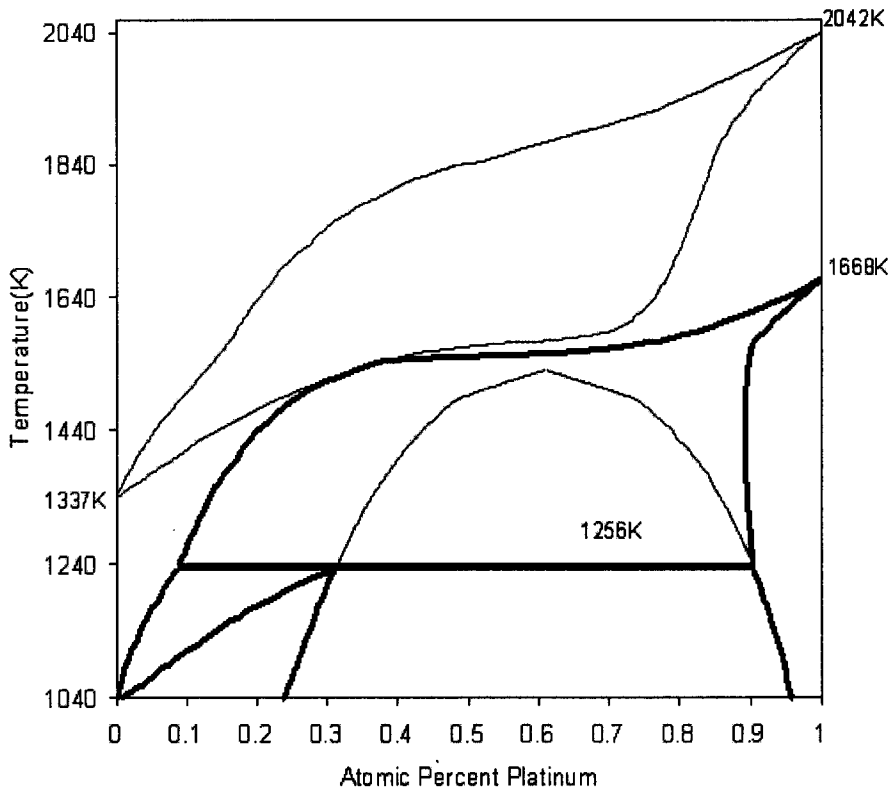


Fig. 5.1. Grain-size dependent phase diagram model, obtained by common tangent line method. The light solid line represents the phase diagram of bulk materials; the strong solid line stands for the phase diagram model with grain size 10nm.

## 5.2 Melting Temperature of Multilayers

In this section, melting temperature of Au-50%Pt multilayers is studied. Theoretical approach and results will be explained as following.

At the equilibrium melting temperature $T_m$, the free energies of solid and liquid are equal. Okmoto and Massalski (1985) presented thermodynamic function for the liquid phase of Au-Pt system, which is given in equation (5.1).

The Gibbs free energy of multilayers can be divided into two parts. One is Gibbs free energy of multilayers without surface energy, considered as the total free energy before mixing; the other is surface energy (interfacial free energy and grain boundary energy).

The Gibbs energy of multilayers without surface energy can be written as

$$G_M^{'} = (1-x)G_{Au} + xG_{Pt} \tag{5.3}$$

where $x$ is the mole fraction of Pt, $G_{Au}$ and $G_{Pt}$ are the mole free energies of pure Au and pure Pt.

Thus, the Gibbs energy of multilayers with surface energy is given by

$$G_M = G_M^{'} + \Delta G_b + \Delta G_\sigma \tag{5.4}$$

where $\Delta G_b$ and $\Delta G_\sigma$ are grain boundary energy and interfacial free energy. Provided average grain size is 6nm, surface energy can be estimated using Au/Pt multilayer model (chapter 4.4.1.2).

Thus, combining equations (5.1) and (5.3), we find that the melting temperature of the multilayers, without considering surface energy, is 1470K. Combining equations (5.1) and (5.4), we attain the melting temperature of multilayers with surface energy is 1300K. Fig.5.2 illustrates the Gibbs free energy curves for solid, liquid solution and multilayers in Au-Pt system at different melting temperatures. Fig.5.2(a) shows the Gibbs free energy curves for Au/Pt multilayers without surface energy at 1470K. S and L represent the free energy curves of solid solution and liquid solution. The line represents the free energy of multilayers without surface energy. The melting point decreases after

we take into account of surface energy. Fig.5.2(b) shows that the Gibbs free energy curves at melting temperature1300K. The distance between A and B denotes the surface energy.

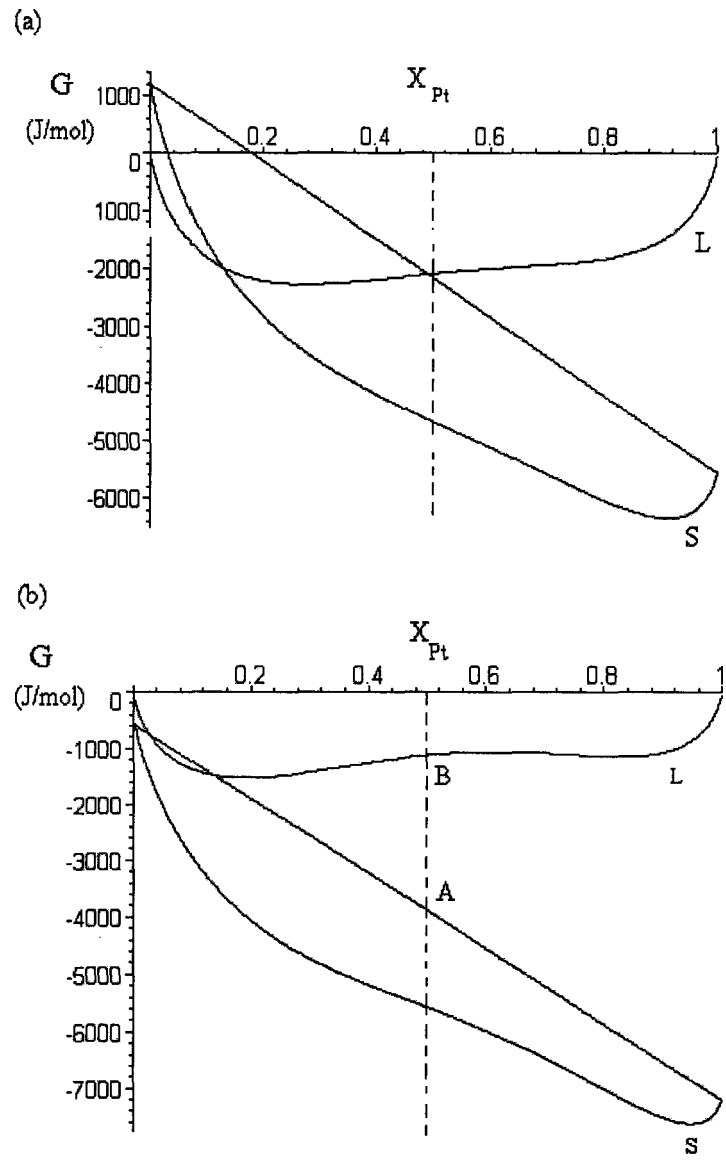


Fig.5.2 Gibbs free energy curves for solid solution, liquid solution and multilayers in Au-Pt system at equilibrium melting temperature. (a) multilayers without surface energy at 1470K. S and L represent the free energies of solid solution and liquid solution. The line represents the free energy of multilayers without surface energy. (b) multilayers with surface energy at 1300K. The AB distance is the surface energy when average grain size is 6nm.

## 5.3 Laser Ablation Experiments

An experimental study of melting temperature of multilayers will be presented in this section. Laser ablation is an interesting attempt to heat multilayers near the melting temperature. A brief introduction of laser technique will be presented first; experimental design and details are followed.

### 5.3.1. Introduction to Laser Ablation Techniques

Laser ablation plays an important role in laser processing and phase transformations of materials. According to pulse duration, the laser can be divided into two classes: ultrashort laser (picosecond and femtosecond) and long pulse laser (conventional continuous wave and nanosecond). The laser parameters typically include pulse energy, spot size, pulse duration and laser wavelength and repetition rate.

Laser ablation implies the removal of macroscopic amount of matter from the surface of solid material. Usually, the material undergoes a change of the fundamental state of aggregation, and transforms into gas or plasma. The transition from the solid phase to the gas phase can occur with melting of the solid and evaporating of the liquid.

The simple damage morphology of single pulse diagram was drawn in Fig 5.3. The intensity distribution fits a Gaussian distribution. As the incident laser energy increases, surface cleaning, slip lines, ripple patterns, flat melting, and boiling damage are generated in succession.

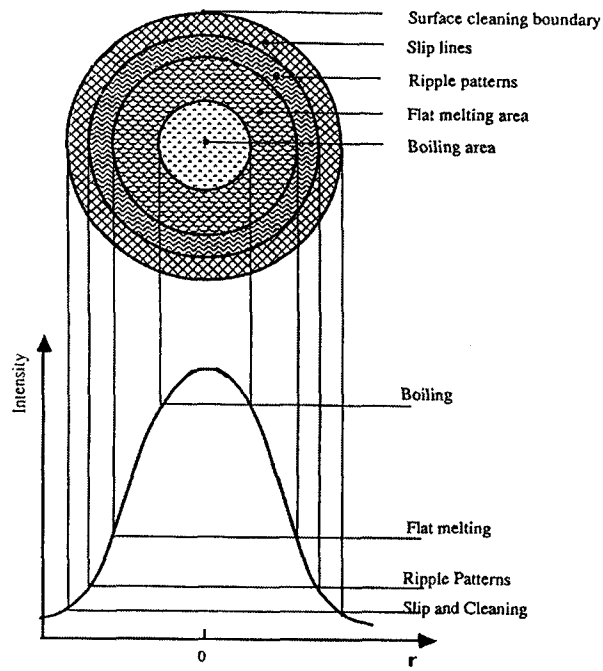


Fig.5.3 The single-pulse morphology.

### 5.3.2. Experimental Design

The expected heat treatment of multilayers immediately gives rise to a question: that of a possible modification of multilayers. The question is particularly open in two cases: one is the formation of solid solution; the other is grain growth. Thus, to prevent any modification of multilayers, a fast heating rate is required. The attractive feature of laser technique is the high heating speed, which keeps multilayers from any transition.

The major drawback may lie in the qualitative nature of information. For example, the melting temperature of multilayers was not measured.

Therefore, it is a qualitative experiment. The melting temperature of multilayers can be qualitatively analyzed by comparing to pure Au and pure Pt, which are set up as parallel temperature references.

### 5.3.3 Experimental Details

The surfaces of pure Au and Pt and multilayers ($5mm \times 3mm \times 100\mu m$) were polished. The sample was placed into a small vacuum chamber ($p < 0.1$bar) mounted on a precision, computer-controlled xyz translation stage. The laser ablation experiments were performed with a commercial 1 kHz amplified Ti: sapphire laser system (Spectra Physics Spitfire). The femtosecond laser produced 145fs pulses centered on a wavelength of 800nm. The nanosecond laser produced 8nm pulses centered on a wavelength of 800nm. The spot size of laser is $5\mu$m. The pulse energy was from $10\mu$J to $0.1\mu$J, which was measured with a calibrated semiconductor power meter. The ablation process was monitored on-line with a CCD camera. The microstructure of the samples was analyzed with scanning electron microscopy (Philips SEM 515).

### 5.3.4 Experimental Results and Discussion

(1) Single Pulse Morphology

Single pulse morphologies of Au/Pt multilayers, pure Au and pure Pt were analyzed with SEM. The typical irradiated regions of multilayers generated by femtosecond laser ablation with different pulse energies are shown in Fig.5.4. The process of femtosecond laser ablation involves non-equilibrium heating and cooling. Fig.5.4 (a) illustrated boiling area generated in the central crater. As pulse energy decreasing, the squared diameter of crater decreases correspondingly (Fig.5.4b and Fig.5.4c). Fig 5.4(d) shows flat-melting region. The annealing temperature of this region is near the melting temperature.

Fig.5.5 shows the irradiated regions of multilayers generated by nanosecond laser ablation with different pulse energy. The surface irradiated by the nanosecond laser is smoother than that of the femtosecond laser ablation. The process of nanosecond laser ablation is more of a thermal process than femtosecond laser ablation.

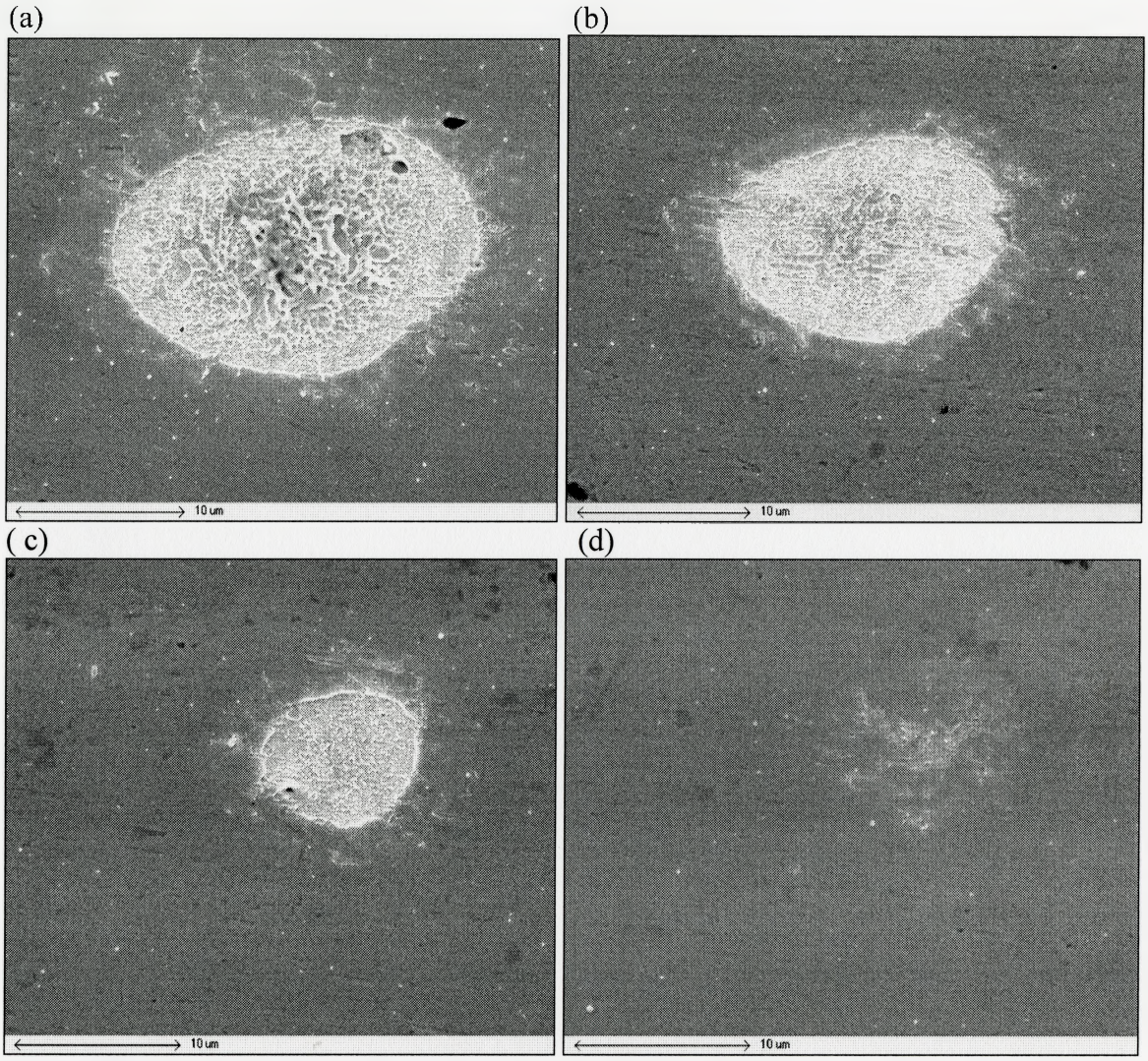


Fig.5.4 (a)-(d) SEM images of single pulse femtosecond laser ablation of Au/Pt multilayers with different pulse energies. (a) 10μJ, (b) 2.8μJ (c) 0.6μJ (d) 0.2μJ

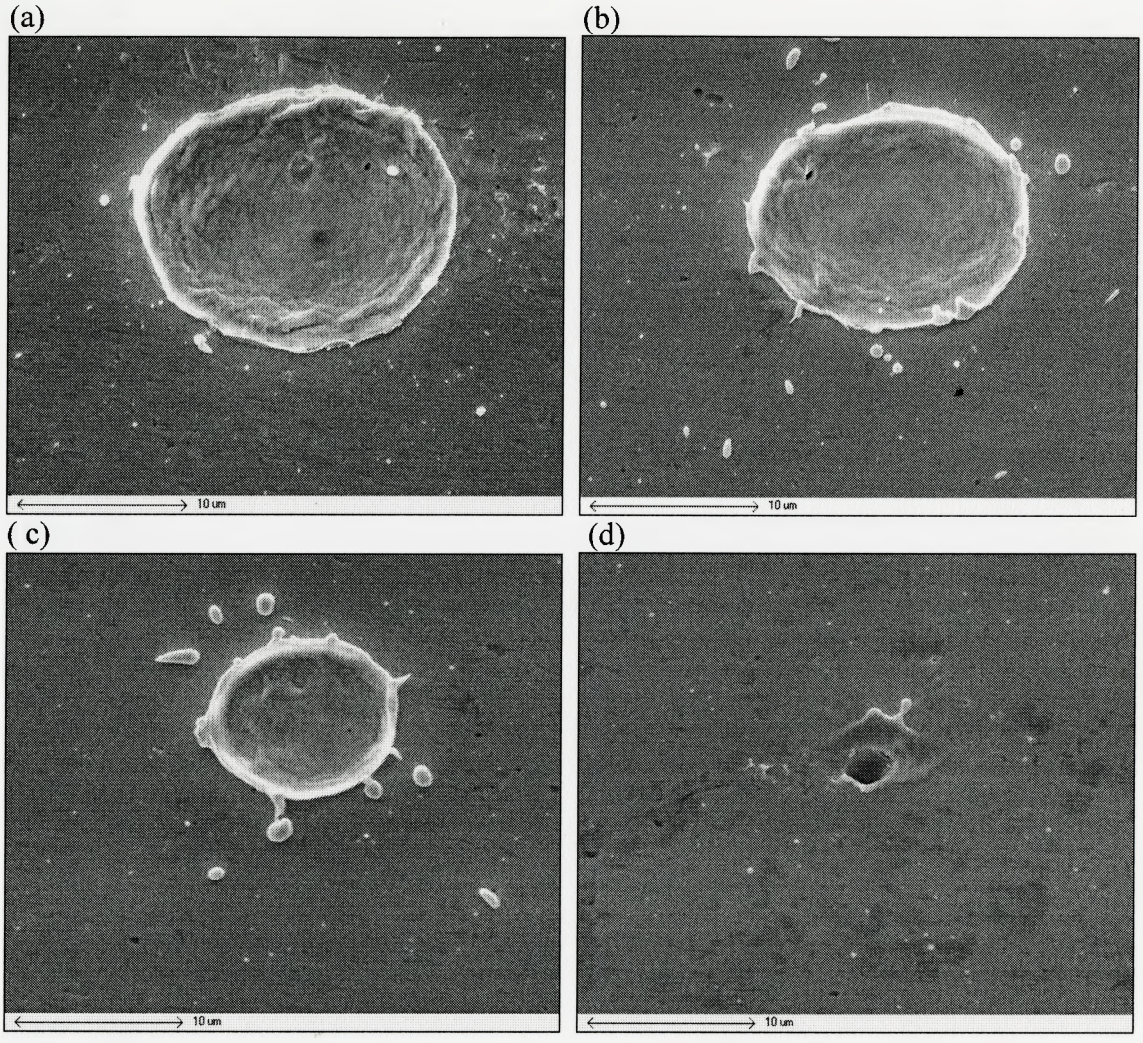


Fig.5.5 (a)-(d) SEM images of single pulse nanosecond laser ablation of Au/Pt multilayers with different pulse energies. (a) 10μJ, (b) 5.7μJ (c) 2.6μJ (d) 1.1μJ

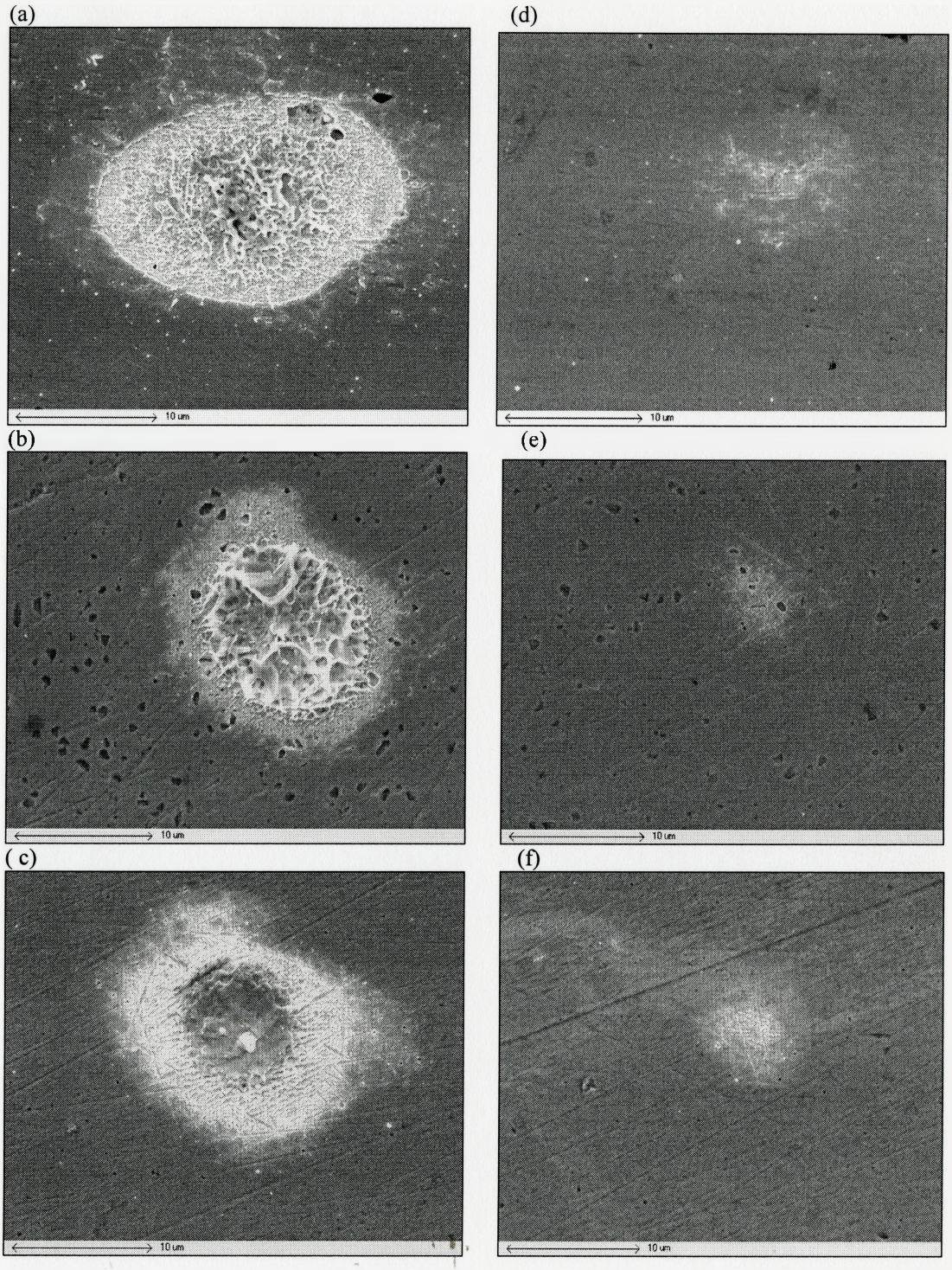


Fig.5.6 (a)-(c) SEM images of single pulse energy 10μJ of femtosecond laser ablation of different materials. (a) Multilayers (b) Au (c) Pt. (d)-(f) SEM images of pulse energy 0.2μJ of single pulse femtosecond laser ablation of different materials (d) Multilayers (e) Au (f) Pt.

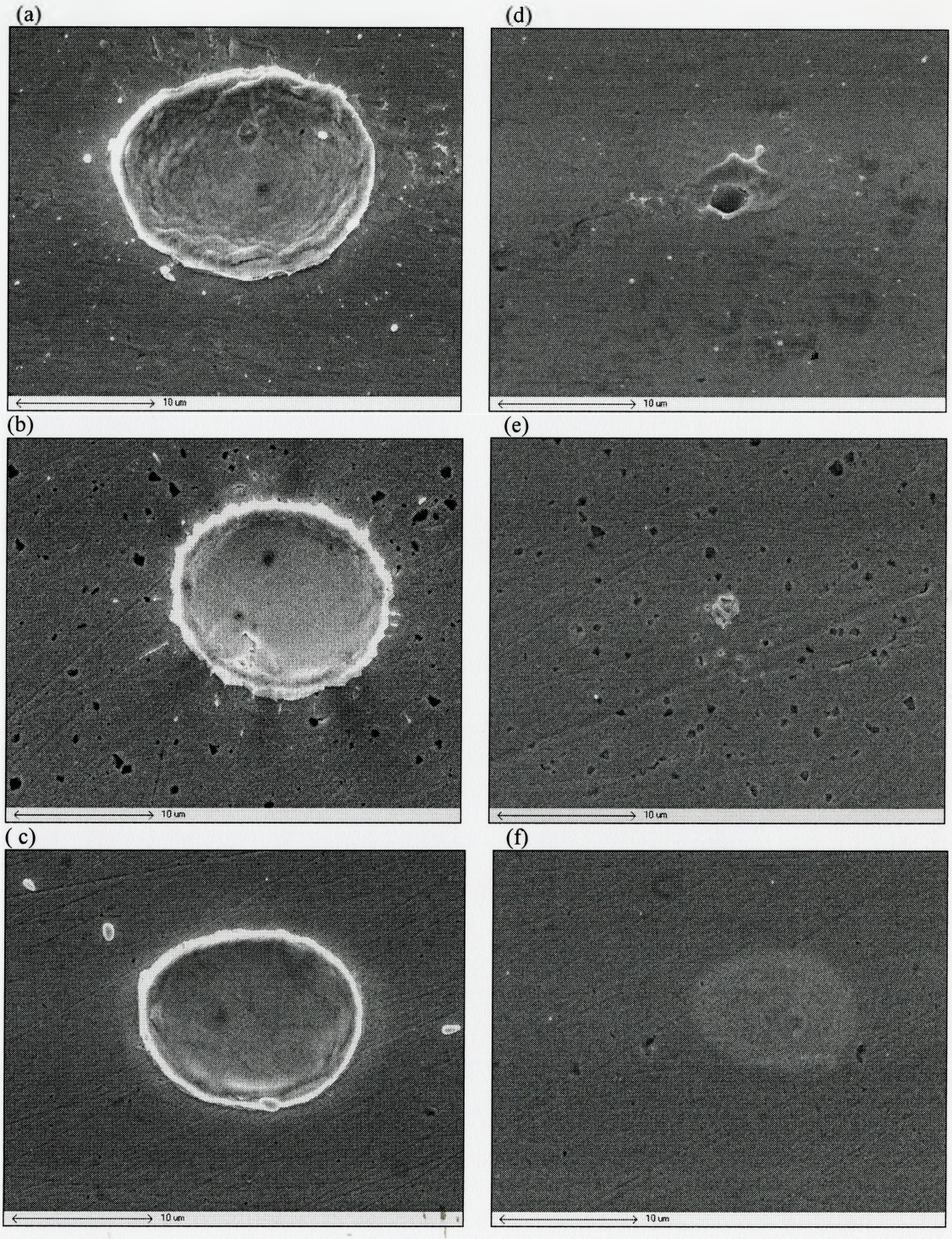


Fig.5.7 (a)-(c) SEM images of single pulse energy 10μJ of nanosecond laser ablation of different materials. (a) Multilayers (b) Au (c) Pt. (d)-(f) SEM images of pulse energy 1.1μJ of single pulse nanosecond laser ablation of different materials (d) Multilayers (e) Au (f) Pt.

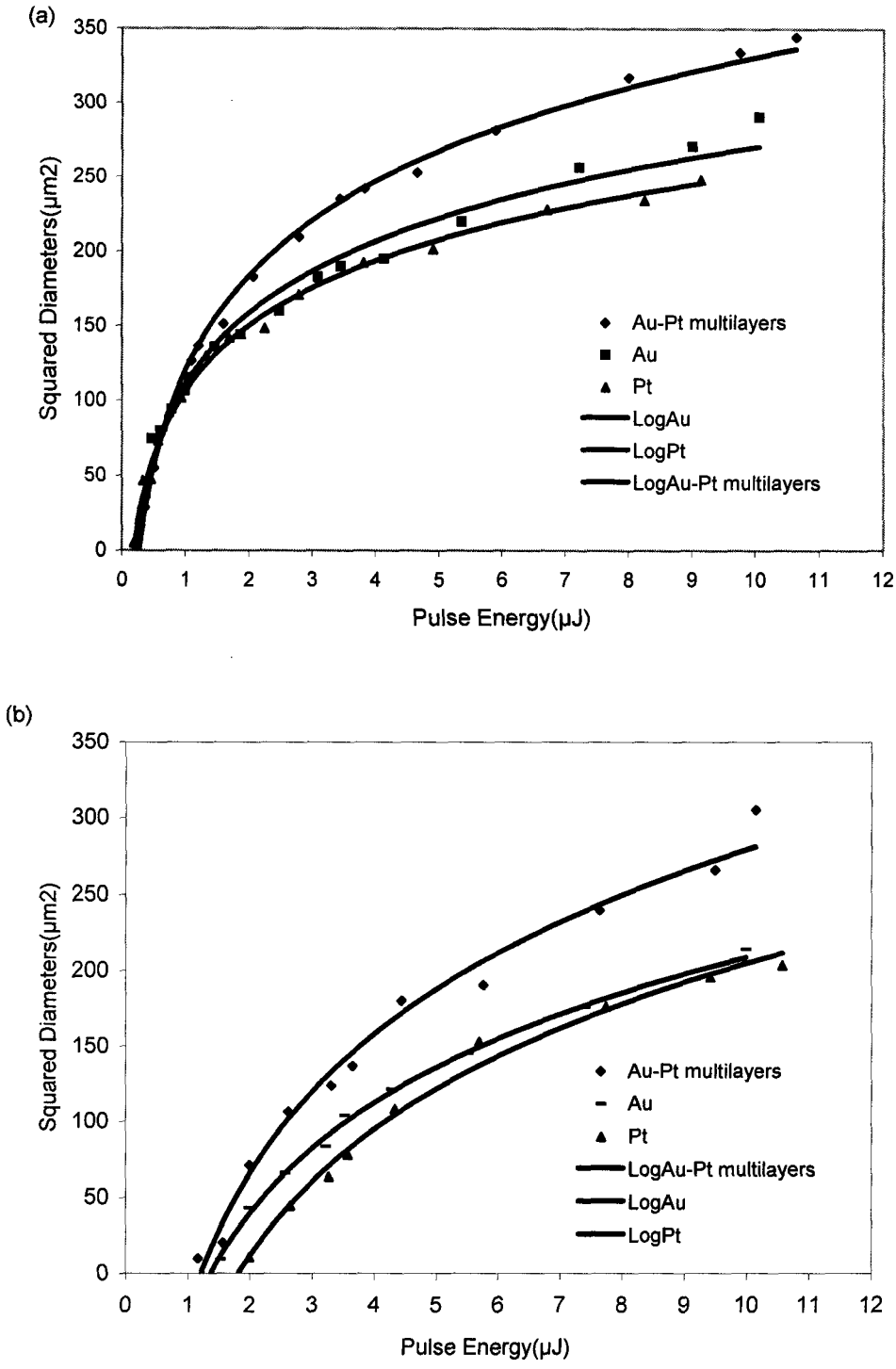


Fig.5.8 Squared diameter of single pulse ablation craters as a function of the pulse energy. (errors: 5% pulse energy measurement,4% diameter measurement) (a) femtosecond laser ablation (b) nanosecond laser ablation

(2) Comparison with Au and Pt

At pulse energy 10μJ, femtosecond laser-produced surfaces of multilayers, Au and Pt are shown in Fig.5.6, as (a), (b), (c) respectively, and results of pulse energy 0.2μJ are shown as Fig.5.6 (d), (e), (f). In the similar way, at pulse energies 10μJ and 1.1μJ, the nanosecond laser irradiant morphologies of multilayers, Au and Pt are shown in Fig5.7. Fig.5.6 and Fig.5.7 clearly demonstrated that crater diameters of multilayers are bigger than Au and Pt at same pulse energy.

Fig.5.8 shows the squared diameter of single pulse ablation craters as a function of the pulse energy. At the same pulse energy, squared diameters of multilayers are much bigger than Au and Pt. It implies that the multilayers are easier to melt than Au and Pt. Consequently, the melting temperature of the multilayers is lower than that of pure Au and Pt. We draw this conclusion with the assumption that Au, Pt and multilayers have similar reflectivity. In this experiment, Au, Pt and multilayers have shining surfaces, thus it is assumed that they have similar reflectivity. The qualitative study is a good starting-point. Further study on this subject is recommended.

## SUMMARY

In this work, regular Au/Pt multilayers have been formed by repeated cold rolling. Thermodynamic property of the multilayers has also been studied. A number of interesting results are summarized as following:

- The most important result is that an unstable Au-50%Pt solid solution is formed during the cold rolling process. The stored interface energy is higher than the energy barrier for the formation of the solid solution. Thus, the solid solution can form even at room temperature during a relatively gentle rolling process. The multilayers are believed to be discontinuously homogenized by the steady state deformation-enhanced coupled diffusion and motion of grain boundaries. Moreover, the solid solution is so unstable that it decomposes into Au and Pt after DSC heating to 500°C at 50°C/min.

- Well-welded and uniform Au/Pt multilayers with average grain size 6nm have been fabricated by the repeated cut-stack-anneal-rolling process.

- The bulk Au-Pt phase diagram is strongly modified at the nanometer scale because of the contribution of interface energy. A grain-size dependent phase diagram model predicts a significant melting-point depression of Au and Pt. A lowered melting point of the multilayers is obtained by theoretical and qualitative experimental approaches.

# FUTURE WORK

In this work, we have been concerned with thermal stability of multilayers. The results offered have been predominantly thermodynamic, rather than kinetic. Much remains to be learned about the kinetics of multilayer homogenization by coupled deformation, grain boundary diffusion and migration, and about the interrelationships between interfacial structure and kinetics. Klinger, Brechet and Purdy (1997) have investigated theoretically several postulated processes for discontinuous homogenization of multilayers in the absence of bulk diffusion. Both the velocity and the shape of the moving grain boundary are investigated. Many interesting results are still open to experimental investigation. It is perhaps worth emphasizing that the initiation transients are less well studied. Special consideration would be given to the beginning process such as initial motion of grain boundary in response to driving forces.

The recently developed technique for precisely controlled growth, Molecular Beam Epitaxy, could be used to grow multilayers with ideal geometry on a bicrystal substrate. It is recommended for further experimental investigation.

According to theoretical treatments of Klinger, Brechet and Purdy (1998), the mechanical properties, especially the fracture behaviour, should be profoundly affected by nanometer-scale multilayer structures. Further experimental study of the mechanical properties of the multilayers is recommended.

## BIBLIOGRAPHY


Battezzati, L., Gallino, I. (1999), Acta Mater. 47, 1901.

Buttner, F. H. (1953), J. Metals, Feb, 313.

Cahn, J. W. (1959), Acta Met. 7,18.

Cahn, J. W., Hilliard, J. E. (1958), J. Chem. Phys, 28,2,258.

Cahn, J. W., Allen, S. (1977), J. Phys, c 7,12, 57.

Cline, H. E. (1971), Acta Met. 19, 481.

Courtney, T. H. (1995), Materials Transactions, JIM, 36,2,110.

Cullity, B. D. (1977), *Elements of X-ray diffraction*, 2nd ed. Addison-Wesley, p.281.

Defay, R., Prigogine, I. (1950), Bull.Soc.Chim.Belegs 59, 255.

Dinsdale, A. T. (1991), CALPHAD, 15, 4, 317.

Fournelle, R. A. (1979), Acta Met. 27, 1147.

Gleiter, H. (1995), *Materials Science Forum*, vol.189-190, Switzerland: Trans Tech, p.67.

Gleiter, H. (2000), Acta Mater. 48, 1.

Graham, L. D., Kraft, R. W. (1966), Trans. Met. Soc. A.I.M.E. 236, 94.

Guggenheim, E. A. (1945), Trans.Faraday Soc. 41,150.

Hillert, M., Purdy, G. R. (1978), Acta Met., 26, 333.

Hirsch, P. B., Howie, A., Nicholson, R. B., Pashley, D. W. (1965), *Electron microscopy of thin crystals*, London: Butterworths, p. 40.

Kaur, I., Gust, W. (1988), *Fundamental of Grain boundary and Interphase Boundary Diffusion*. Stuttgart: Ziegler.

Kaya, M. and Smith, R. W. (1989), Acta Met. 37, 6,1657.

Klinger, L., Brechet, Y., Purdy, G. (1997), Acta Mater. 45, 4667.

Klinger, L., Brechet, Y., Purdy, G. (1998), Acta Mater. 46, 2617.

Livingston, J. D., Cahn, J. W. (1974), Acta Met. 22, 495.

Mclean, M., Honddros, E. D. (1971), J. Materials Science, 6, 19.

Murr, L. E. (1975), *Interfacial Phenomena in Metals and alloys,* Addoson-Wesley, p.130.

Okamoto, H., Massalski, T. B. (1985), Bull. Alloy phase Diagrams, 6, 298.

Pawlowski, A., Zieba, P. (1991), *Phase Transformations Controlled by Diffusion at Moving Boundaries*, Krakow, Poland: Polish Academy of Sciences, ARCHIVES OF METALLURGY.

Perepezko, J. H. (2001), Acta Mater. 49, 1139.

Peterson, N. L. (1983), *International Metals Reviews,* 28, 65.

Purdy, G. (1971), Met.Sci.J. 5, 81.

Purdy, G. (1993), *Materials Science and Technology,* vol.5, Weinheim: VCH, p.305.

Purdy, G., Brechet, Y. (2002), *Phase Transformation in Materials, chapter7,* Weinheim: Wiley-VCH, p.481.

Shaw, L . L. (2000), Decemer.JOM, 41.

Siegel, R. W. (1994), *Nanophase Materials, Encyclopedia of Applied physics,* vol.11, Weinheim: VCH, p.173.

Vanderstraeten, H., Neerinck, D., (1991), J. Appl.Cryst. 24, 571.

Wautelet, M., Dauchot, J.P., Hecq, M. (2000), Nanotechnology, 11, 6.

Weatherly, G. C. and.Nakagawa, Y. G. (1971), Scripta Met, 5, 777.

Xu, M., Yang, T. (2001), J. Phys., Condens. Matter, 13, 2891.

Yasuna, K., Terauchi, M. (1997), J. Appl. Phys, 82, 1, 2345.

## Appendix 1: Lattice Parameter Measurement

The lattice parameter $a$ of cubic crystal is directly proportional to the spacing $d$ of any particular set of lattice planes. If we measure the Bragg angle $\theta$ for the set of planes (hkl), we can use the Bragg law to determine $d$ and, knowing $d$, we can calculate $a$. $d$ can be determined by equation (1.1), where $\lambda$ is the wavelength. Lattice parameter $a$ can be given by equation (1.2).

$$d = \frac{\lambda}{2\sin\theta} \tag{1.1}$$

$$a = d \times \sqrt{h^2 + k^2 + l^2} \tag{1.2}$$

(1) Sample after 14 cut-rolling cycles

$$a = \frac{0.154nm}{2\sin(32.88)} \times \sqrt{2^2 + 2^2 + 0^2} = 0.4011nm$$

(2) Sample after 14 cut-rolling cycles and heating to 500°C at 50°C/min

$$a = \frac{0.154nm}{2\sin(32.6)} \times \sqrt{2^2 + 2^2 + 0^2} = 0.4042nm$$

## Appendix 2: Grain Size Measurement

Scherrer formula is used to estimate the grain size neglecting microstrain. It is given by equation (2.1),

$$B = \frac{0.9\lambda}{t\cos\theta} \tag{2.1}$$

where $B$ is the broadening of diffraction line measured at half its maximum intensity, $t$ is the small grain size, and $\lambda$ is the wavelength.

Instrument broadening correction term may be written as

$$B^2 = B_M^2 - B_S^2 \tag{2.2}$$

where $B_s$ is the measured breadth at half-maximum intensity of standard line of pure Pt, and $B_M$ is the measured breadth of the diffraction line.

Combining equations (2.1) and (2.2), the grain size t is given by

$$t = \frac{0.9\lambda}{\cos\theta\sqrt{B_M^2 - B_S^2}} \tag{2.3}$$

The measured data from the diffraction curve of the sample after 14 cut-rolling cycles are listed in Table A1:

| $B_M$ (Degree) | $B_M$ (Radian) | $B_s$ (Degree) | Bs (Radian) | θ (Degree) | λ (angstrom) |
|---|---|---|---|---|---|
| 1.630 | 0.028456 | 0.3913 | 0.006823 | 33.727 | 1.54 |

Table A1 XRD data of Au/Pt multilayers after 14 cut-rolling cycles

Applying data into equation (2.3), we get grain size $t = 6.032(nm)$

## Appendix 3: Driving Force to Form Solid Solution

```
> restart;
```

f is solid Gibbs free energy per mole of Au-Pt system at 298K, x is mole fraction of Pt

```
f:=((-11300000+9.7711900*2988)*(1-x) + (-
19650+9.6224*298))*x+(8.3144*2988*(x*ln(x))+(1-x)*ln(1-x)))+x*(1-x)*(30000*x-
(-113+14.183*x))*298));
```

$$f := -10103.7380 - 6678.7868\,x + 2477.572\,x\ln(x) + 2477.572\,(1-x)\ln(1-x) + x(1-x)\,(25773.466\,x + 3874.)$$

G1 is molar Gibbs free energy of Au-50% Pt at 298K

```
> G1:=evalf(subs(x=0.5,f));
```

$$G1 := -10970.27020$$

To get the common tangent line T=mx+a, x1,x2 are the equilibrium compositions lie on common line

```
dfdx:=diff(f,x);
```

$$dfdx := -6678.7868 + 2477.572\ln(x) - 2477.572\ln(1-x) + (1-x)\,(25773.466\,x + 3874.) - x\,(25773.466\,x + 3874.) + 25773.466\,x\,(1-x)$$

```
> mf1:=subs(x=x1,dfdx);
```

$$mf1 := -6678.7868 + 2477.572\ln(x1) - 2477.572\ln(1-x1) + (1-x1)\,(25773.466\,x1 + 3874.) - x1\,(25773.466\,x1 + 3874.) + 25773.466\,x1\,(1-x1)$$

```
> mf2:=subs(x=x2,dfdx);
```

$$mf2 := -6678.7868 + 2477.572\ln(x2) - 2477.572\ln(1-x2) + (1-x2)\,(25773.466\,x2 + 3874.) - x2\,(25773.466\,x2 + 3874.) + 25773.466\,x2\,(1-x2)$$

```
>sols:=fsolve({mf1=mf2,(subs(x=x2,f)-subs(x=x1,f)))/(x2-
x1)=mf1},{x1=0..0.1,x2=0.9..1});
```

$$sols := \{x1 = .07178842823,\ x2 = .9999943193\}$$

```
>assign(sols);
> f1:=evalf(subs(x=x1,f));
```

$$f1 := -10841.57384$$

```
> f2:=evalf(subs(x=x2,f));
```

$$f2 := -16782.50251$$

```
>m:=(f2-f1)/(x2-x1);
```

$$m := -6400.442754$$

```
> B:=f2=m*x2+a;
```

$$B := -16782.50251 = -6400.406395 + a$$

```
>a:=solve(B,a);
```

$$a := -10382.09612$$

```
> T:=m*x+a;
```

$$T := -6400.442754\,x - 10382.09612$$

G2 is an equilibrium free energy of Au-50%Pt alloy

```
> G2:=evalf(subs(x=0.5,T));
```

$$G2 := -13582.31750$$

G3 is the driving force to form solid solution Au-50%Pt per mole at 298K.

```
> G3:=evalf(G1-G2);
```

$$G3 := 2612.04730$$

## Appendix 4: Coherent Interfacial Free Energy of Au-Pt system at 298K

```
> restart;
> f:=(1.67e-17)*((-13000+9.7190*298)*x+(-19650+9.6224*298)*x+(8.3144*298*((x*ln(x))+((1-x)*ln(1-x))))+x*(1-x)*(30000*x-((-13+14.183*x)*298)));
```

$$f := -.1687324246\ 10^{-12} - .1115357396\ 10^{-12}\,x + .413754524\ 10^{-13}\,x\ln(x) + .413754524\ 10^{-13}\,(1-x)\ln(1-x) + .167\ 10^{-16}\,x\,(1-x)\,(25773.466\,x + 3874.)$$

```
> dfdx:=diff(f,x);
```

$$dfdx := -.1115357396\ 10^{-12} + .413754524\ 10^{-13}\ln(x) - .413754524\ 10^{-13}\ln(1-x) + .167\ 10^{-16}\,(1-x)\,(25773.466\,x + 3874.) - .167\ 10^{-16}\,x\,(25773.466\,x + 3874.) + .4304168822\ 10^{-12}\,x\,(1-x)$$

```
> mf1:=subs(x=x1,dfdx);
```

$$mf1 := -.1115357396\ 10^{-12} + .413754524\ 10^{-13}\ln(x7) - .413754524\ 10^{-13}\ln(1-x7) + .167\ 10^{-16}\,(1-x7)\,(25773.466\,x7 + 3874.) - .167\ 10^{-16}\,x7\,(25773.466\,x7 + 3874.) + .4304168822\ 10^{-12}\,x7\,(1-x7)$$

```
> mf2:=subs(x=x2,dfdx);
```

$$mf2 := -.1115357396\ 10^{-12} + .413754524\ 10^{-13}\ln(x2) - .413754524\ 10^{-13}\ln(1-x2) + .167\ 10^{-16}\,(1-x2)\,(25773.466\,x2 + 3874.) - .167\ 10^{-16}\,x2\,(25773.466\,x2 + 3874.) + .4304168822\ 10^{-12}\,x2\,(1-x2)$$

```
>sols:=fsolve({mf1=mf2,(subs(x=x2,f))-subs(x=x1,f))}//(x2-x1)=mf1},{x1=0...0.1,x2=0..9..1});
```

$$sols := \{x7 = .07178842823,\ x2 = .9999943193\}$$

```
> assign(sols);
> f1:=evalf(subs(x=x1,f));
```

$$f1 := -.1810542831\ 10^{-12}$$

```
> f2:=evalf(subs(x=x2,f));
```

$$f2 := -.2802677919\ 10^{-12}$$

```
> m:=(f2-f1)/(x2-x1);
```

$$m := -.1068873940\ 10^{-12}$$

```
> B:=f2=m*x2+a;
```

$$B := -.2802677919\ 10^{-12} = -.1068867868\ 10^{-12} + a$$

```
> a:=solve(B,a);
```

$$a := -.1733810051\ 10^{-12}$$

```
> T:=m*x+a;
```

$$T := -.1068873940\ 10^{-12}\ x - .1733810051\ 10^{-12}$$

```
> df:=(9.3e-29*(f-T))**.5;
```

$$df := (.43231798\ 10^{-42} - .432296138\ 10^{-42}\ x + .3847917073\ 10^{-41}\ x \ln(x) + .3847917073\ 10^{-41}\ (1-x)\ln(1-x) + .15531\ 10^{-44}\ x\ (1-x)\ (25773.466\ x + 3874.))^{.5}$$

```
> plot({df},x=0..1):

> leftbox(df,x=x1+1e-4..x2-1e-4,500):

> zz:=leftsum(df,x=x1+1e-4..x2-1e-4,500):
> evalf(zz);
```

$$.1446084055\ 10^{-20}$$

```
> zz1=2*6.24*e22*evalf(zz); (erg/cm^2)
```

$$zz1 = .1804712901\ 10^{-19}\ e22$$

## Appendix 5: Grain Boundary Energy and Interfacial Free Energy

The total change in the free Gibbs energy of multilayers, neglecting stain energy, can be divided into two parts: interfacial free energy and grain boundary energy. In order to estimate this energy, we first present a simple model: A regular periodic multilayer composed of alternated layers of pure Au and Pt, shown as below. We assume that the system is free of elastic strains, and the layers are of equal thickness *a*. Each grain is cubic and has perfect cube/cube orientation relationship.

(1) Grain Boundary Energy

The grain boundary energy can be written as

$$\Delta G_b = \Delta G_{bAu} + \Delta G_{bPt} \tag{5.1}$$

where $\Delta G_{bAu}$ is the grain boundary energy of Au, $\Delta G_{bPt}$ is the grain boundary energy of Pt. $\Delta G_{bAu}$ is given by

$$\Delta G_{bAu} = \gamma_{Au} \times A_b \times N \tag{5.2}$$

where $\gamma_{Au}$ is the grain boundary energy of Au per unit area, $A_b$ is grain boundary area of per grain, and $N$ is the number of Au/Pt grains in one mole Au-Pt multilayer. $A_b$ is given by

$$A_b = a^2 \times 2 \tag{5.3}$$

In one mole Au-Pt multilayers model, we assume that the number of Au grains $N_{Au}$ is equal to the number of Pt grains $N_{Pt}$. While the $N_{Au}$ and $N_{Pt}$ can be written as

$$N_{Au} = \frac{V_{mAu} \times (1-x)}{a^3} \tag{5.4}$$

$$N_{Pt} = \frac{V_{mPt} \times x}{a^3} \tag{5.5}$$

where $V_{mAu}$ and $V_{mPt}$ are mole volume of Au and Pt. $x$ is the mole fraction of Pt. The values of $V_{mAu}$ and $V_{mPt}$ are given in $V_{mAu} = 10.21(cm^3/mol), V_{Pt} = 9.09(cm^3/mol)$.

Combining equations (5.4) and equation (5.5), and applying $V_{mAu}$ and $V_{mPt}$ into equations, we attain that $x = 0.529(mol), 1-x = 0.471(mol)$. The number of Au/Pt grains of one mole Au-Pt multilayers is given by:

$$N = \frac{4.81 \times 10^{-6}}{a^3} \tag{5.6}$$

Thus, the grain boundary energy can be expressed as:

$$\Delta G_b = 2a^2 N(\gamma_{Au} + \gamma_{Pt}) \tag{5.7}$$

(2) Interfacial Free Energy

The interfacial free energy is the integral of the sum of two contributions: one being incoherent energy, estimated by average grain boundary energies of Au and Pt; the other is coherent interfacial free energy, a term that can be evaluated according to Cahn (1958).

$$\Delta G_\sigma = \Delta G_{coherent} + \Delta G_{incoherent} \tag{5.8}$$

$$\Delta G_{coherent} = 2N_v \int_{c_\alpha}^{c_\beta} [\kappa \Delta f(c)]^{\frac{1}{2}} dc \tag{5.9}$$

where $N_v$ is the number of molecules per unit volume, $c_\beta$ and $c_\alpha$ are equilibrium compositions, $\kappa$ is gradient energy coefficient, $c$ is mole fraction of Pt component, and $\Delta f(c)$ is the free energy per molecule referred to a standard state of an equilibrium mixture.

In this model, $\Delta G_\sigma$ is evaluated by:

$$\Delta G_\sigma = [\sigma + 0.5(\gamma_{Au} + \gamma_{Pt})] \times a^2 \times 2N \tag{5.10}$$

where $\sigma$ is coherent interfacial free energy per unit area, and $a^2 \times 2N$ is the total interface area.

Combining equations (5.7) and (5.10), we get the total change of Gibbs free energy

$$\Delta G = a^2 N[3(\gamma_{Au} + \gamma_{Pt}) + 2\sigma] \tag{5.11}$$

Applying equation (5.6) into equation (5.11), we attain

$$\Delta G = 4.81 \times 10^{-6}[3(\gamma_{Au} + \gamma_{Pt}) + 2\sigma] \times \frac{1}{a} \tag{5.12}$$

Grain boundary energy and interfacial free energy are depended on temperature. The values of grain boundary energies of Au and Pt are listed in Table A2. Table 4.2 shows grain boundary energies of Au and Pt as a function of temperature.

| Metal | Grain boundary energy $\gamma_{gb}$ (erg/cm$^2$) | Temperature (°C) | $d\gamma_{gb}/dT$ (erg/cm$^2$°C) |
|---|---|---|---|
| Au | 365 ±50 | 1000 | -0.10 |
| Pt | 525 ±35 | 1400 | -0.18 |

Table A2 Grain boundary energy as a function of temperature ( Murr,1975, Butter, 1953, Mclean and Honddros, 1971).

For example, we would like to calculate the total change of Gibbs free energy at 298K of multilayers with grain size 6nm. Applying data:

$\gamma_{Au}$ = 475.5(erg/cm$^2$), $\gamma_{Pt}$ = 890(erg/cm$^2$), $\sigma$ = 1800(erg/cm$^2$), $a$ = 6(nm)

into equation (5.12), we can attain $\Delta G = 3572(J/mol)$ In the same way, we can calculate the total change Gibbs free energy with grain size at a different temperatures.

## Appendix 6: Phase Diagram Model

A grain size-dependent phase diagram can be derived from the free energy curves for the solid and liquid phases. The surface energy is added into the Gibbs free energy of solid phase. For example, at peritectic temperature 1256K, equilibrium compositions of solid phase are 0.3211 and 0.8969 mole Pt; equilibrium composition of liquid phase is 0.0926mol Pt. The solution is assigned by Maple software.

```
restart;
>gl:=8.314*T*((xl*ln(xl))+((1-xl))*ln(1-xl)))+xl*(1-xl))*((23500+4000*xl));
```

$$gl := 8.314\,T(xl\,\ln(xl) + (1 - xl)\ln(1 - xl)) + xl(1 - xl)\,(23500 + 4000\,xl)$$

```
>gs:=((-13000+9.7190*T)*(1-x))+(-19650+9.6224*T))*x+(8.314*T*(x*ln(x)+((1-
x))*ln(1-x)))+x*(1-x)*((30000*x-((-13+14.183*x)*T)))+((1157.814*(1-
x))+1799.82*x));
```

$$gs := (-13000 + 9.7190\,T)\,(1 - x) + (-19650 + 9.6224\,T)\,x + 8.314\,T(x\,\ln(x) + (1 - x)\ln(1 - x)) + x(1 - x)\,(30000\,x - (-13 + 14.183\,x)\,T) + 1157.814 + 642.006\,x$$

```
>gAu:=378-0.11*(T-1273);(grain boundary energy as a function of
temperature)
```

$$gAu := 505.3 - .11\,T$$

```
>gPt:=660-0.18*(T-1573);
```

$$gPt := 943.14 - .18\,T$$

```
>gl:=(2.828*6.25*10^22)/(4*1.38*10^(-16))*1533))*((9.3*10^(-
29))^0.5*(2*1.38*10^(-16)))^(1.5))*((1533-T)^(1.5));
```

$$gl := .009235986454\,(1533 - T)^{1.5}$$

```
> G1:=((10^9/10))*4.81*10^(-6))*((3*((gAu+gPt))+gl))*0.001;(total interfacial
free energy and grain boundary energy when average grain size is 10nm)
```

$$Gl := 2090.098920 - .4040400000\,T + .004442509484\,(1533 - T)^{1.5}$$

```
> G:=gs+G1;
```

$$G := (-13000 + 9.7190\,T)\,(1 - x) + (-19650 + 9.6224\,T)\,x + 8.314\,T(x\,\ln(x) + (1 - x)\ln(1 - x)) + x(1 - x)\,(30000\,x - (-13 + 14.183\,x)\,T) + 3247.912920 + 642.006\,x - .4040400000\,T + .004442509484\,(1533 - T)^{1.5}$$

```
>ml:=diff(gl,xl);
```

$$ml := 8.314\,T(\ln(xl) - \ln(1 - xl)) + (1 - xl)\,(23500 + 4000\,xl) - xl\,(23500 + 4000\,xl) + 4000\,xl(1 - xl)$$

```
> ms:=diff(G,x);
```

$$ms := -6007.994 - .0966\,T + 8.314\,T(\ln(x) - \ln(1-x)) + (1-x)(30000\,x - (-13 + 14.183\,x)\,T) - x(30000\,x - (-13 + 14.183\,x)\,T) + x(1-x)(30000 - 14.183\,T)$$

```
> msa:=subs(x=xa,ms);
```

$$msa := -6007.994 - .0966\,T + 8.314\,T(\ln(xa) - \ln(1-xa)) + (1-xa)(30000\,xa - (-13 + 14.183\,xa)\,T) - xa(30000\,xa - (-13 + 14.183\,xa)\,T) + xa(1-xa)(30000 - 14.183\,T)$$

```
> msb:=subs(x=xb,ms);
```

$$msb := -6007.994 - .0966\,T + 8.314\,T(\ln(xb) - \ln(1-xb)) + (1-xb)(30000\,xb - (-13 + 14.183\,xb)\,T) - xb(30000\,xb - (-13 + 14.183\,xb)\,T) + xb(1-xb)(30000 - 14.183\,T)$$

```
> sols:=fsolve({ml=msa,msa=msb,(gl-subs(x=xb,G))/(xl-xb)=msb,(gl-
subs(x=xa,G))/(xl-
xa)=msa},{T,xa,xb,xl},{T=500..1400,xa=0..0.5,xb=0.5..1,xl=0..0.5});
```

$$sols := \{xb = .8968623328,\ xl = .09260192275,\ T = 1256.140999,\ xa = .3211319699\}$$

## Appendix 7: Melting Temperature of Multilayers

### (1) Melting Temperature of Multilayers without Surface Energy

At equilibrium melting temperature, the free energies of solid and liquid are equal. The free energy of multilayers without surface energy is considered as the total free energy before mixing. The melting temperature is 1470K assigned by Maple software.

```
> restart;
> gl:=8.314*T*((x*ln(x) + (1-x)*ln(1-x))+x*(1-x)*(23500+4000*x));
```

$$gl := 8.314\,T(x\ln(x) + (1-x)\ln(1-x)) + x(1-x)(23500 + 4000\,x)$$

```
> gll:=evalf(subs(x=0.5,gl));
```

$$gll := -5.762825660\,T + 6375.000$$

```
> gs:=(-13000+9.7190*T)*(1-x) + (-19650+9.6224*T)*x+(8.314*T*(x*ln(x) + (1-
x)*ln(1-x)))+x*(1-x)*(30000*x-(-13+14.183*x)*T));
```

$$gs := (-13000 + 9.7190\,T)(1-x) + (-19650 + 9.6224\,T)\,x + 8.314\,T(x\ln(x) + (1-x)\ln(1-x)) + x(1-x)(30000\,x - (-13 + 14.183\,x)\,T)$$

```
> gs1:=evalf(subs(x=0.5,gs));
```

$$gs1 := -12575.000 + 5.384999340\,T$$

```
> G:=(1-x)*(-13000+9.7190*T)+x*(-19650+9.6224*T);
```

$$G := (-13000 + 9.7190\,T)(1-x) + (-19650 + 9.6224\,T)\,x$$

```
> G1:=evalf(subs(x=0.5,G));
```

$$G1 := -16325.0 + 9.67070\,T$$

```
> sols:=fsolve({gl1=G1},T,{T=0..2000});
```

$$sols := \{T = 1470.824004\}$$

**(2) Melting Temperature of Multilayers with Surface Energy**

The surface energy is added into the free energy of solid phase. The melting temperature is 1300K assigned by Maple software.

```
> restart;
> gl:=8.314*T*(x*ln(x)+(1-x)*ln(1-x))+x*(1-x)*(23500+4000*x);
```

$$gl := 8.314\,T(x\ln(x) + (1-x)\ln(1-x)) + x(1-x)(23500 + 4000\,x)$$

```
> gl1:=evalf(subs(x=0.5,gl));
```

$$gl1 := -5.762825660\,T + 6375.000$$

```
> gs:=(-13000+9.7190*T)*(1-x)+(-19650+9.6224*T)*x+(8.314*T*(x*ln(x)+(1-
x)*ln(1-x))+x*(1-x)*(30000*x-(-13+14.183*x)*T));
```

$$gs := (-13000 + 9.7190\,T)(1-x) + (-19650 + 9.6224\,T)\,x + 8.314\,T(x\ln(x) + (1-x)\ln(1-x)) + x(1-x)(30000\,x - (-13 + 14.183\,x)\,T)$$

```
> gs1:=evalf(subs(x=0.5,gs));
```

$$gs1 := -12575.000 + 5.384999340\,T$$

```
> G:=(1-x)*(-13000+9.7190*T)+x*(-19650+9.6224*T);
```

$$G := (-13000 + 9.7190\,T)(1-x) + (-19650 + 9.6224\,T)\,x$$

```
> G1:=evalf(subs(x=0.5,G));
```

$$G1 := -16325.0 + 9.67070\,T$$

```
> g(Au):=378-0.1*(T-1273);
```

$$g(Au) := 505.3 - .1\,T$$

```
> g(Pt):=660-0.18*(T-1573);
```

$$g(Pt) := 943.14 - .18\,T$$

```
> g(I):=(2.828*6.25*10^22)/(4*1.38*10^(-16)*1533)*(9.3*10^(-
29))^0.5*(2*1.38*10^(-16))^(1.5)*(1533-T)^(1.5);
```

$$g(I) := .009235986454\ (1533 - T)^{1.5}$$

```
>G2:=(10^9/6)*4.81*10^(-6)*(3*(g(Au)+g(Pt)))+g(1))*0.001;
```

$$G2 := 3483.498200 - .6734000000\ T + .007404182474\ (1533 - T)^{1.5}$$

```
> sols:=fsolve({gll=Gl+G2},T,{T=0..2000});
```

(the Gibbs free energy of liquid gll is equal to the Gibbs free energy of multialyers with surface energy at 0.5mole Pt, Gl is the gibbs free energy of multilayers without surface energy term, G2 is the surface free energy)

$$sols := \{T = 1300.137403\}$$